From source to surface: clues from garnet-bearing Carboniferous silicic volcanic rocks, Iberian Pyrite Belt, Portugal

A. Cravinho, D. Rosa, J. M. R. S. Relvas, A. R. Solá, Inês Pereira, Jean-Louis Paquette, M. L. Borba, C. C. G. Tassinari, D. Chew, F. Drakou, et al.

Contributions to Mineralogy and Petrology (2024) 179:32
https://doi.org/10.1007/s00410-024-02106-3

ORIGINAL PAPER

From source to surface: clues from garnet-bearing Carboniferous silicic volcanic rocks, Iberian Pyrite Belt, Portugal

A. Cravinho[1] · D. Rosa[2] · J. M. R. S. Relvas[1] · A. R. Solá[3] · I. Pereira[4,5] · J.-L. Paquette[5] · M. L. Borba[6] · C. C. G. Tassinari[6] · D. Chew[7] · F. Drakou[7] · K. Breiter[8] · V. Araujo[9]

Received: 4 October 2023 / Accepted: 24 January 2024 / Published online: 19 March 2024

Abstract

This work investigates the relationships between partial melting, melt extraction, pluton growth and silicic volcanism in garnet-bearing felsic volcanic rocks that were extruded in the Iberian Pyrite Belt, at ca. 345 Ma. The garnets are of peritectic origin, displaying textural and chemical features of disequilibrium crystallization during partial melting reactions involving biotite at high temperatures (up to 870 °C) in the middle-lower crust. Major element composition suggests compositional equilibrium with the entrained and pinitized peritectic cordierite, but reveals some subsequent homogenization by diffusion. Trace element maps and spot analyses of garnet show, nonetheless, significant trace element variations, reflecting biotite and Y-REE-P-rich accessory phase breakdown during partial melting reactions. Peritectic garnet and cordierite growth resulted in the preservation of Th- and Y-rich prograde suprasolidus monazite, which constrains the timing of partial melting of the metapelitic protolith at *ca.* 356.8 ± 2.4 Ma. The zircon cargo further shows that a significant amount of zircon crystals from previously crystallized felsic melts were also remobilized and erupted. These were likely stored in an upper crustal pluton that grew episodically since ca. 390 Ma during voluminous melt generation periods within the middle to lower crust, which also resulted in voluminous volcanism. The geochemical trends of the felsic volcanic rocks reflect the entrainment of xenoliths of peritectic garnet, cordierite and feldspar, and as such, the garnet-bearing felsic volcanic rocks represent an erupted mixture of a lower-temperature (*ca.* 770 °C) silicic melt and autocrysts, and peritectic phases and zircon crystals from previously crystallized and stored felsic melts.

Keywords Peritectic garnet · Prograde monazite · Peraluminous rhyolites · Petrogenesis · Iberian Pyrite Belt

Communicated by Dante Canil.

J.-L. Paquette—deceased.

✉ A. Cravinho
acravinhosantos@gmail.com

[1] Faculdade de Ciências, Instituto Dom Luiz (IDL), Universidade de Lisboa, Lisbon, Portugal

[2] Department of Mapping and Mineral Resources, Geological Survey of Denmark and Greenland (GEUS), 1350 Copenhagen, Denmark

[3] Laboratório Nacional de Energia e Geologia (LNEG), Unidade de Geologia e Cartografia Geológica, Amadora, Portugal

[4] Universidade de Coimbra, Centro de Geociências, Departamento de Ciências da Terra, 3030-790 Coimbra, Portugal

[5] CNRS, IRD, OPGC, Laboratoire Magmas et Volcans, Université Clermont Auvergne, 63170 Clermont-Ferrand, France

[6] Instituto de Geociências, Universidade de São Paulo, Rua do Lago, 562, São Paulo 05508-900, Brazil

[7] Department of Geology, School of Natural Sciences, Trinity College Dublin, Dublin 2, Ireland

[8] Institute of Geology of the Czech Academy of Sciences, Rozvojová 269, 16500 Prague 6, Czech Republic

[9] Sociedade Mineira de Neves Corvo SOMINCOR, Castro Verde, SA, Portugal

Introduction

Crustal-derived water-undersaturated and peraluminous felsic plutonic and volcanic rocks, broadly corresponding to S-type granites of Chappell and White (1992), represent a major component of the upper continental crust. They are typically generated by partial melting of a metasedimentary crust under variable temperature and pressure conditions, involving the breakdown of muscovite and biotite (Clemens et al. 2020; Johnson et al. 2021).

Experimental work and petrology studies on upper amphibolite- to granulite-facies metasedimentary migmatites and plutons in the lower and middle crust have provided deep insights into partial melting and melt extraction in the crust (e.g., Brown 2013; Clemens et al. 2020), whereby melt is generated via incongruent fluid-present or fluid-absent melting reactions. These commonly generate peritectic phases found in melt-depleted migmatites (e.g., Taylor et al. 2010; Rocha et al. 2017; Charette et al. 2021), which can be entrained and transported during segregation and extraction from the source (Taylor and Stevens 2010). Peritectic phases are not common in felsic plutons, as entrained peritectic phases may be rapidly assimilated into the melt (Clemens et al. 1997) or react with the host melt, generating other stable phases (Lavaure and Sawyer 2011; Rong et al. 2017). Nevertheless, numerous works have identified compositionally and texturally modified peritectic phases in felsic plutons (Erdmann et al. 2009; Villaros et al. 2009a; Taylor and Stevens 2010; Lavaure and Sawyer 2011; Dorais and Tubrett 2012; Jung et al. 2022; Dorais and Campbell 2023). The geochemical variation in major and trace elements of felsic plutonic and volcanic rocks has thus been increasingly interpreted as resulting from the entrainment and assimilation of peritectic phases (e.g., Stevens et al. 2007; Villaros et al. 2009b; Farina et al. 2012; Clemens et al. 2017b; Garcia-Arias and Stevens 2017; Zhu et al. 2020, 2021; Bailie et al. 2020).

The relationship between felsic plutons and volcanic rocks (the volcanic–plutonic relation), however, remains debated (e.g., Clemens et al. 2022). The most common view encountered in the literature is that felsic volcanic rocks represent melts (and their corresponding crystal cargo) extracted from crystallizing silicic crystal mushes (e.g., Bachmann et al. 2007; Wallrich et al. 2023). Other studies have shown that felsic melts can form and extrude from incrementally emplaced plutons without evidence of significant fractionation in crustal reservoirs, and preserve source-inherited geochemical signatures (e.g., Clemens et al. 2011a, 2017b; Fiannacca et al. 2017). The major challenge in linking the petrogenesis of felsic volcanic rocks to source-related processes is the scarcity of preserved peritectic phases (e.g., garnet) and granulite-facies xenoliths in the volcanic record, although they have been reported (Harangi et al. 2002; Cesare et al. 2009; Acosta-Vigil et al. 2010).

Garnet-bearing felsic volcanic rocks are found in the Cotovio area in the Iberian Pyrite Belt (IPB), the most important tectonostratigraphic unit of the South Portuguese Zone (SPZ) (Fig. 1). These garnet-bearing volcanic rocks are part of a suite of voluminous crustal-derived felsic magmas erupted in the IPB during the Paleozoic, but their

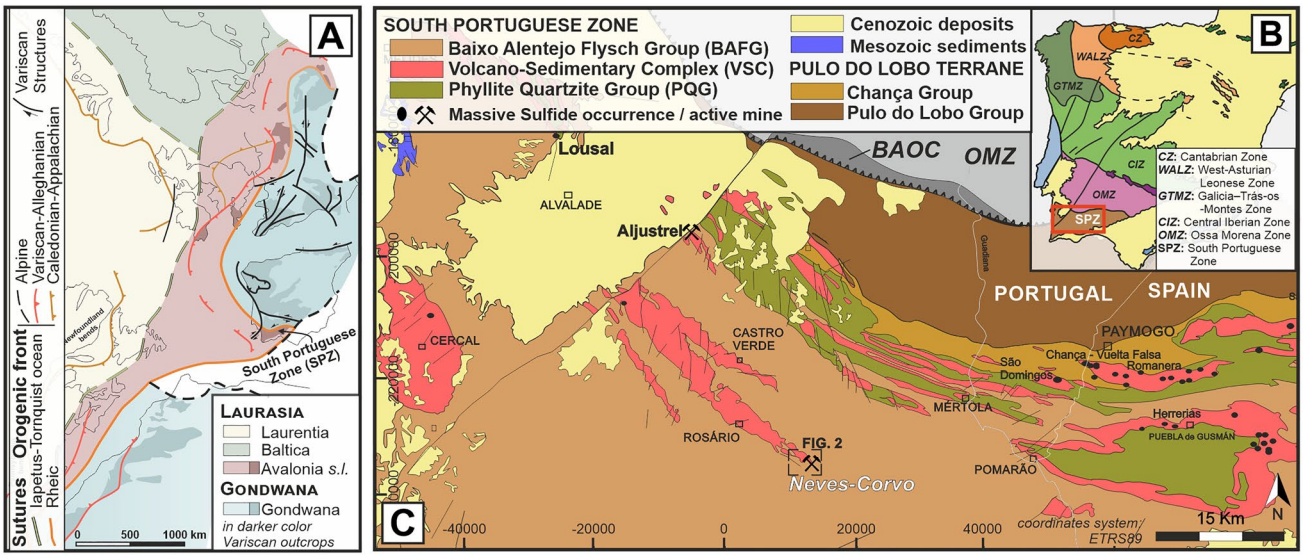

Fig. 1 **A** Simplified paleogeographic reconstruction showing the South Portuguese Zone before the fragmentation of Pangea (adapted from Pastor-Galán et al. 2020); **B** map of the Iberian Terrane (adapted from Ribeiro et al. 2010); **C** geological map of the South Portuguese Zone, adapted from Luz et al (2021)

petrogenesis is yet to be fully understood. This work aims to identify the origin of garnet crystals and constrain the petrogenesis of these garnet-bearing felsic volcanic rocks, providing insights into the source to surface evolution of this crustal-derived magmatism.

Geological background

The closure of the Rheic Ocean during the Variscan orogeny culminated with the collision of Gondwana with Laurasia, whose suture can be found from Central America through Central Europe (Nance et al. 2012). In SW Iberia, the suture separates the Ossa Morena Zone (OMZ), the northern margin of Gondwana, and the SPZ on the Laurasian side (Fig. 1A; Ribeiro et al. 2007; Braid et al. 2011b).

The SPZ–OMZ collision developed under an oblique tectonic setting, generating transtensional pull-apart basins (Oliveira 1990; Quesada 1991; Tornos et al. 2002), which constitute one of the biggest volcanogenic massive sulfide (VMS) metallogenic districts in the world—the Iberian Pyrite Belt (IPB) (Tornos et al. 2002). These basins were infilled by a siliciclastic-dominated stratigraphic sequence (up *to* 5–10 km thick), with ages ranging from the Middle Devonian up to the Carboniferous (Pereira et al. 2007; Mendes et al. 2020). These sediments were derived from eroded crustal basement, possibly the Meguma terrane (Braid et al. 2011, 2012; Luz et al. 2021). From the Visean onward, the SPZ was deformed and metamorphosed under low-grade metamorphic conditions, up to lower-greenschist facies, generating a SW-verging thin-skinned fold–thrust belt (Munhá 1990; Abad et al. 2001).

Crustal-derived felsic volcanic rocks (rhyolites to dacites) often dominate the bimodal volcanism in the IPB (Mitjavila et al. 1997; Tornos 2006), although mafic volcanic and subvolcanic intrusive rocks can be voluminous in some sectors. Intermediate clinopyroxene-bearing volcanic rocks also crop out in the IPB and formed by crustal contamination and/or mixing of mantle-derived mafic magmas with crustal-derived felsic melts (Mitjavila et al. 1997; Codeço et al. 2018; Donaire et al. 2020a). U–Pb age dating of the felsic volcanic rocks in the IPB indicate that magmatism spanned from ca. 380 to 335 Ma (Rosa et al. 2009; Oliveira et al. 2019; Albardeiro et al. 2023).

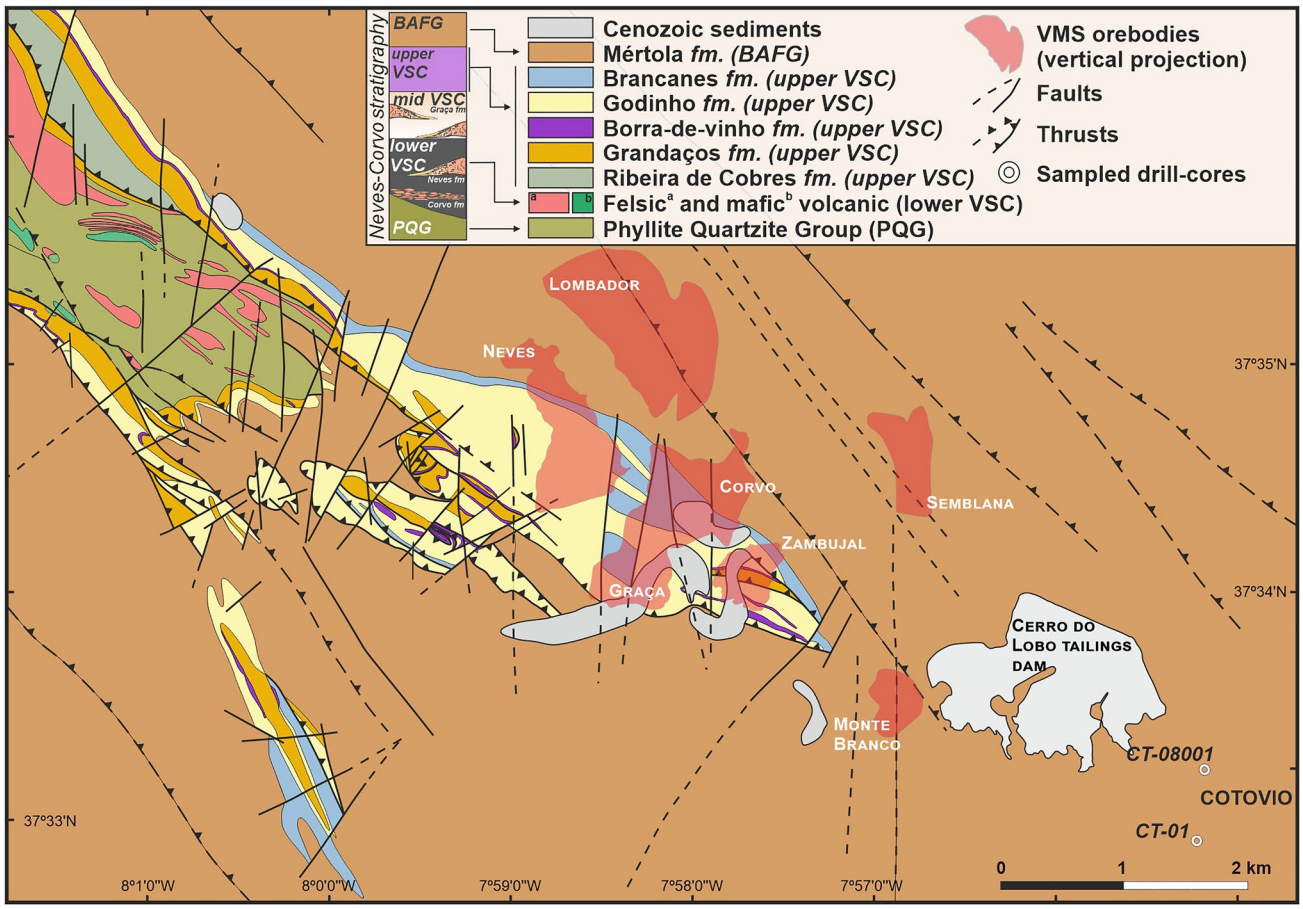

Fig. 2 Geological map of the Neves-Corvo area, adapted from Pereira et al. (2021) with a simplified lithostratigraphic column of the area

The Rosário–Neves-Corvo anticline (Figs. 1C, 2) represents a SW-verging major Variscan structure in the SPZ (Oliveira et al. 2004, 2013). The anticline gently plunges to the SE, and associated deformation comprises intense foliation near thrust faults with associated folding and moderate foliation development elsewhere in a thin-skinned deformation style. The stratigraphy in the Neves-Corvo area resembles the classical IPB stratigraphic sequence comprising from bottom to top: (i) the phyllite–quartzite group (PQG), of Givetian–Fammenian age (as old as *ca.* 387–384 Ma), with abundant sandstones, graywackes, mudstones and marls (Oliveira et al. 2004; Mendes et al. 2020); (ii) the volcano-sedimentary complex (VSC), dominated by Late Famennian to Visean (*ca.* 366–332 Ma) pelitic rocks (Oliveira et al. 2004; Pereira et al. 2021) with abundant felsic volcanic rocks of rhyolitic to dacitic composition, representing effusive felsic domes/cryptodomes and explosive volcanic pyroclastic deposits (Rosa et al. 2008; Oliveira et al. 2013); and (iii) the Baixo Alentejo Flysch Group (BAFG), deposited during the Visean, and composed of siliciclastic flysch-type turbidites (Pereira et al. 2007). In the SE termination of the Rosário anticline, two mineral exploration drill holes intersected a thick garnet-bearing felsic volcanic unit in the hanging wall stratigraphic sequence of the giant Sn-rich Cu–Zn Neves-Corvo VMS deposit (Carvalho et al. 2017) (Fig. 2).

Results

Volcanic facies and petrography

The garnet-bearing felsic volcanic rocks comprise thick and massive, variably muscovite- and chlorite-altered quartz–feldspar–phyric rhyolites (Fig. 3; Electronic Supplementary Material ESM 1). The volcanic sequence is dominated by the jigsaw-fit and clast-rotated breccia facies (Fig. 3). These consist of thick intervals of massive and poorly sorted clast-supported and clast- to matrix-supported breccias, respectively, with angular and blocky clasts set in a fine-grained matrix composed of quartz, feldspar and microphenocrysts fragments. Coherent intervals of microporphyritic and massive facies are less thick (up to a few meters) and are enclosed by the jigsaw-fit and clast-rotated breccia facies, with gradational contacts (Fig. 3). This volcanic facies association is typical of submarine felsic effusive lava flows and cryptodomes and is common throughout the IPB, where coherent volcanic

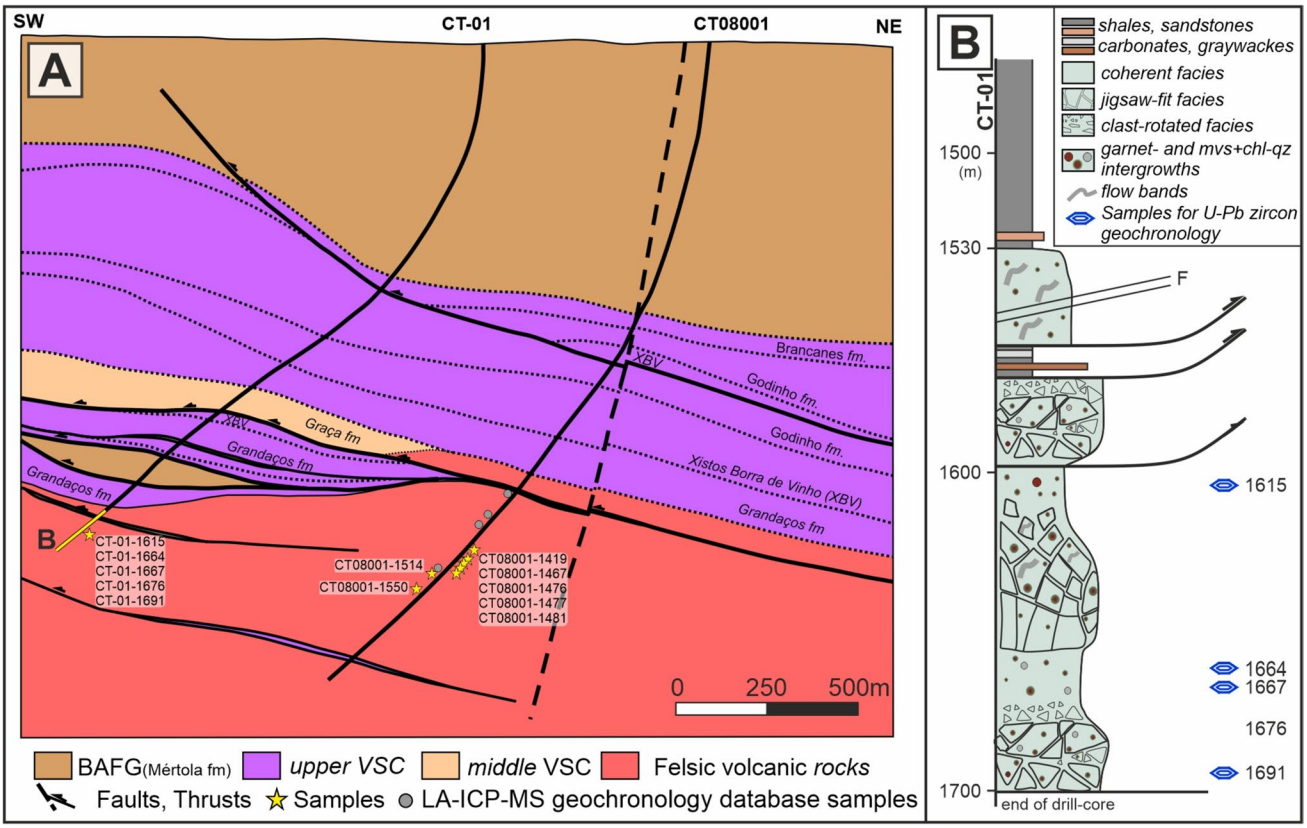

Fig. 3 **A** Geological cross section of the Cotovio area (adapted from Carvalho et al. 2017); **B** Detailed volcanic facies characterization of the CT-01 drill core

rocks are enveloped within hyaloclastites and thick in situ autobreccias, resulting from quenching and interaction with seawater, with minor sedimentary transport and reworking (e.g., McPhie et al. 1993; Rosa et al. 2008; Donaire et al. 2020b).

The matrix of the coherent volcanic rocks, devoid of fiamme, comprises micropoikilitic quartz feldspar (recrystallized volcanic glass) and muscovite, which also outlines the relict perlitic fractures (Fig. 4A, B). Phenocrysts account for up to 15%$_{vol}$. Quartz phenocrysts are common and are up to 0.5 mm in size (average 100 µm). They have rounded and embayed anhedral shapes (Fig. 4B–D), which display undulose extinction and are commonly mantled by fine-grained quartz. Variably sized (up to 4 mm) euhedral–subhedral porous and "dusty" albitized (?) feldspars are also abundant, and variably replaced by epidote (Fig. 4A–E) and muscovite. Epidote is also found as rounded crystal aggregates, replacing spherulites and the felsic matrix. Quartz and feldspars, although commonly found as individual microphenocrysts, are also found as rounded to subhedral crystal aggregates and as glomerocrysts. Biotite is rare, occurring as chloritized/altered rounded microphenocrysts dispersed within the groundmass, exhibiting oxide-rich (opacitic) rims (Fig. 4C). Euhedral zircon crystals are common inclusions in feldspars (Fig. 4A), and are also found within the groundmass. Other accessory mineral phases include apatite and monazite, both disseminated in the matrix and as inclusions in feldspars. Primary oxide phases in the matrix and as inclusions in feldspars are often intensely replaced by TiO_2 (rutile) + titanite ± chlorite (ESM1 Sfigs 1.3N). Rare sulfides (pyrite ± chalcopyrite ± sphalerite) are found within the matrix and associated with apatite + chlorite + epidote + monazite + sulfides and carbonate veinlets and fractures. The matrix in the clast-rotated and jigsaw-fit breccias resembles the matrix in the coherent volcanic facies and is composed of abundant microcrystalline quartz and feldspar with fragments of quartz and feldspar microphenocrysts, but it is more fine-grained, and muscovite and chlorite are more abundant. Regardless of the volcanic facies, variably sized garnets are common (Figs. 4, 5; ESM1).

Garnet textures

Garnet in the felsic volcanic rocks is found dispersed in the matrix as poikiloblastic garnet–quartz intergrowths (Figs. 4, 5 Electronic Supplementary Material 1), quartz-free euhedral to subhedral garnet crystals (Fig. 5), or as crystal fragments.

Poikiloblastic garnet–quartz crystal intergrowths are sub-rounded to subhedral, sometimes with well-developed garnet crystal faces (Fig. 4F, G, H) and are up to 0.5 cm diameter. These garnets are characterized by abundant elongated, filmy, rounded, euhedral, lobate to cuspate quartz intergrowths and inclusions (Figs. 4F–I, 5A, B). Rounded and irregular polycrystalline inclusions are found in the quartz intergrowths, possibly representing crystallized melt inclusions. Parts of the quartz intergrowths in garnet display optical continuity. Another feature of the garnet–quartz intergrowths is the common presence of amalgamated garnet–quartz interlocking crystal aggregates (Fig. 4G). Quartz-free garnet grains are smaller (up to 0.1 cm diameter) and display subhedral to euhedral shapes (Fig. 5C-G).

Garnets contain small (< 40 µm) inclusions of euhedral–subhedral zircon and monazite (Figs. 4, 5), and occasionally inclusions of small aggregates (pseudomorphs?) of rutile, titanite and/or minor chlorite (ESM1.3, SFigs. B, F, I, J, M), which sometimes also have apatite and quartz inclusions. Inclusions occur in the core, mantle and near the rims of the garnet–quartz intergrowths and quartz-free euhedral garnets (Figs. 4, 5; ESM1). Furthermore, garnet crystals are variably replaced by chlorite or chlorite and muscovite (Figs. 4, 5C, E, F). In zones where garnets are intensely replaced, abundant rounded and irregularly shaped monazite is sometimes found, with occasional minor allanite, rutile, and apatite.

Other rounded muscovite–chlorite–quartz intergrowths are also rarely found (Fig. 5H, I). They are texturally similar to the garnet–quartz intergrowths in size (up to 0.3 cm), comprising rounded, lobate, and cuspate quartz, partially in optical continuity (Fig. 5H, I), intergrown with a parent phase which is completely altered to fine-grained aggregates of a muscovite and chlorite rich pseudomorph (pinite). These occur as complex replacements along microfractures that grew inward into the pseudomorphed phase (cordierite?) (Fig. 5H, I; ESM1). Accessory phases such as zircon, monazite, apatite and minor allanite are also found within the pseudomorphic aggregates (Fig. 5H).

Garnet major and trace element composition

The complete garnet EPMA and LA-ICP-MS dataset can be found in ESM2 Table 1, additional LA-ICP-MS trace-element profiles in ESM3, and analytical methods are provided in ESM4. All garnets are FeO-rich and MgO-, MnO-, and CaO-poor, almandine-pyrope solid solution garnets, with minor spessartine and grossular components (between $Alm_{0.90–0.80}Pyr_{0.10–0.04}Sps_{0.05–0.01}Grs_{0.03–0.01}$) (EPMA data in ESM2 Table 1). Garnets intergrown with quartz show major element zoning, with preserved normal prograde growth zoning characterized by rimward increases in X_{Alm} (0.85 up to 0.90) and X_{Pyr} (0.05 up to 0.06) and decreases in X_{Sps} (0.03 down to 0.01) and X_{Grs} (0.02–0.01) (Fig. 6A, B). Quartz-free, euhedral garnets are characterized by similar compositions, but differ from the garnet intergrown with quartz by having lower X_{Sps}

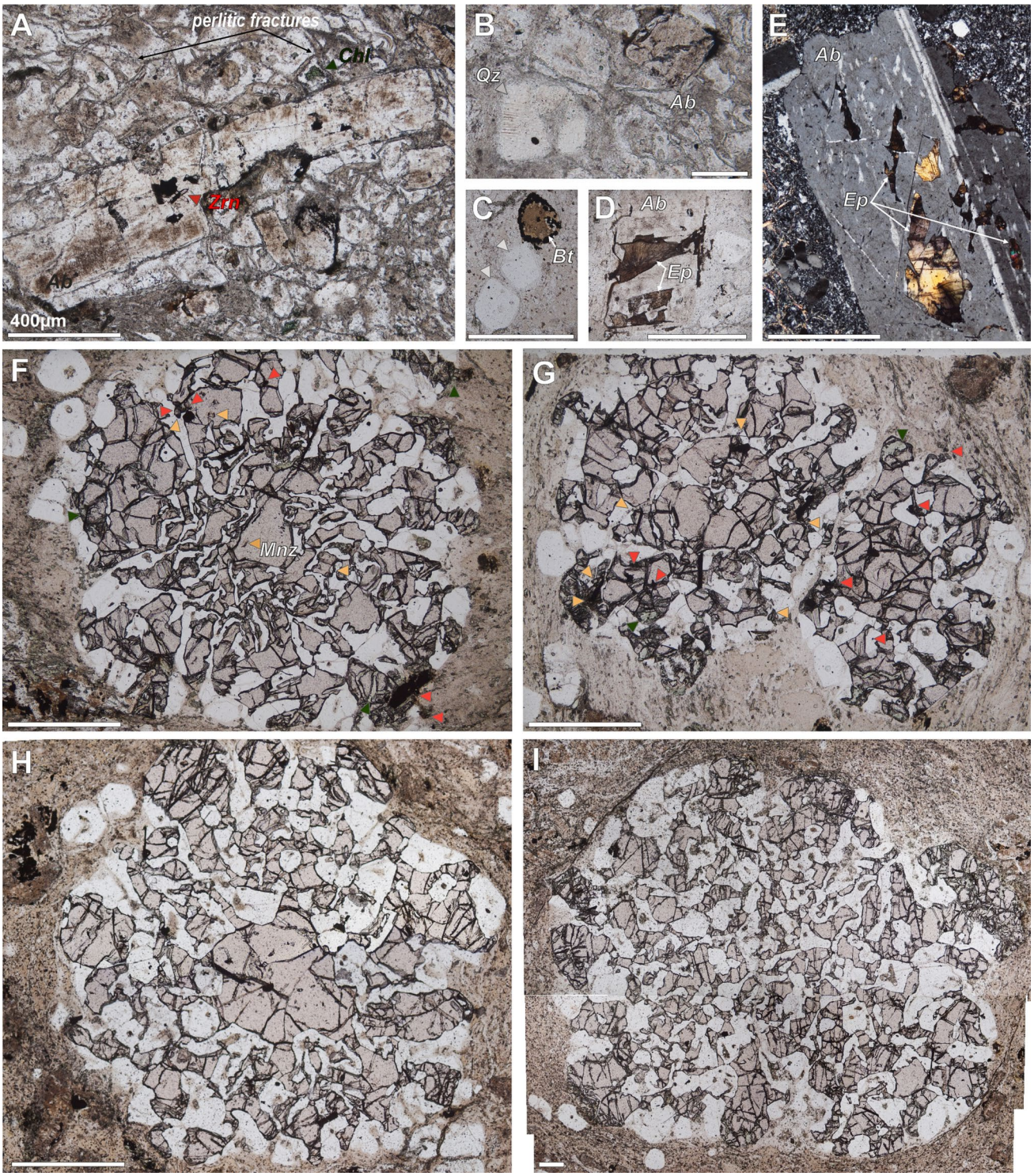

Fig. 4 Photomicrographs of the garnet-bearing silicic volcanic rocks. Red arrows represent zircon inclusions, orange arrows are monazite inclusions in garnet and quartz, and dark-green arrows are chlorite. Scale bars are 400 µm. **A** Zircon inclusions in a feldspar phenocryst (albite), set in a quartz- and K-feldspar-rich matrix with abundant perlitic fractures; **B** Embayed quartz and euhedral feldspar microphenocrysts. **C** Rounded biotite with opaque rims and quartz microphenocrysts. **D** and **E** Epidote replacing feldspars, **F** to **I** rounded to subhedral garnet intergrown with quartz, displaying filmy, elongated and lobate quartz inclusions. Note in **G** the presence of two amalgamated garnet–quartz intergrowths

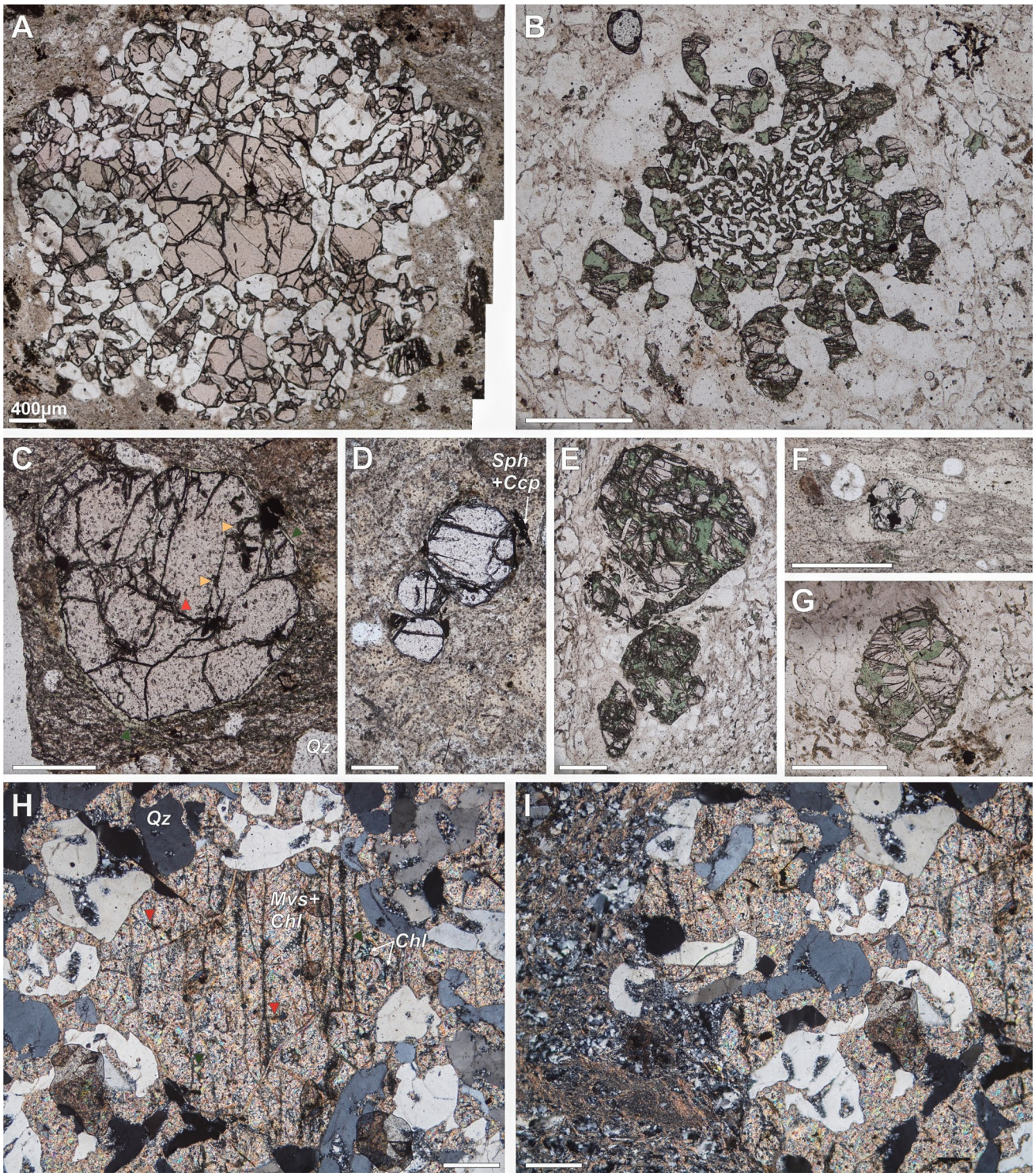

Fig. 5 Photomicrographs of the garnet-bearing silicic volcanic rocks. Red arrows are zircon inclusions, orange arrows are monazite inclusions in garnet and quartz and green arrows are chlorite. Scale bars are 400 µm. **A** Garnet intergrown with quartz displaying a quartz-free core and filmy and lobate quartz inclusions and intergrowths in the mantle and rim (trace element map in Fig. 7). **B** Chlorite-altered garnet intergrown with lobate quartz intergrowths, **C** to **G** smaller, euhedral quartz-free garnets, variably replaced by chlorite. **H** and **I** Muscovite–chlorite pesudomorphs intergrown with quartz. Note that quartz is not entirely in optical continuity, a similar feature to the garnet–quartz intergrowths and inclusions

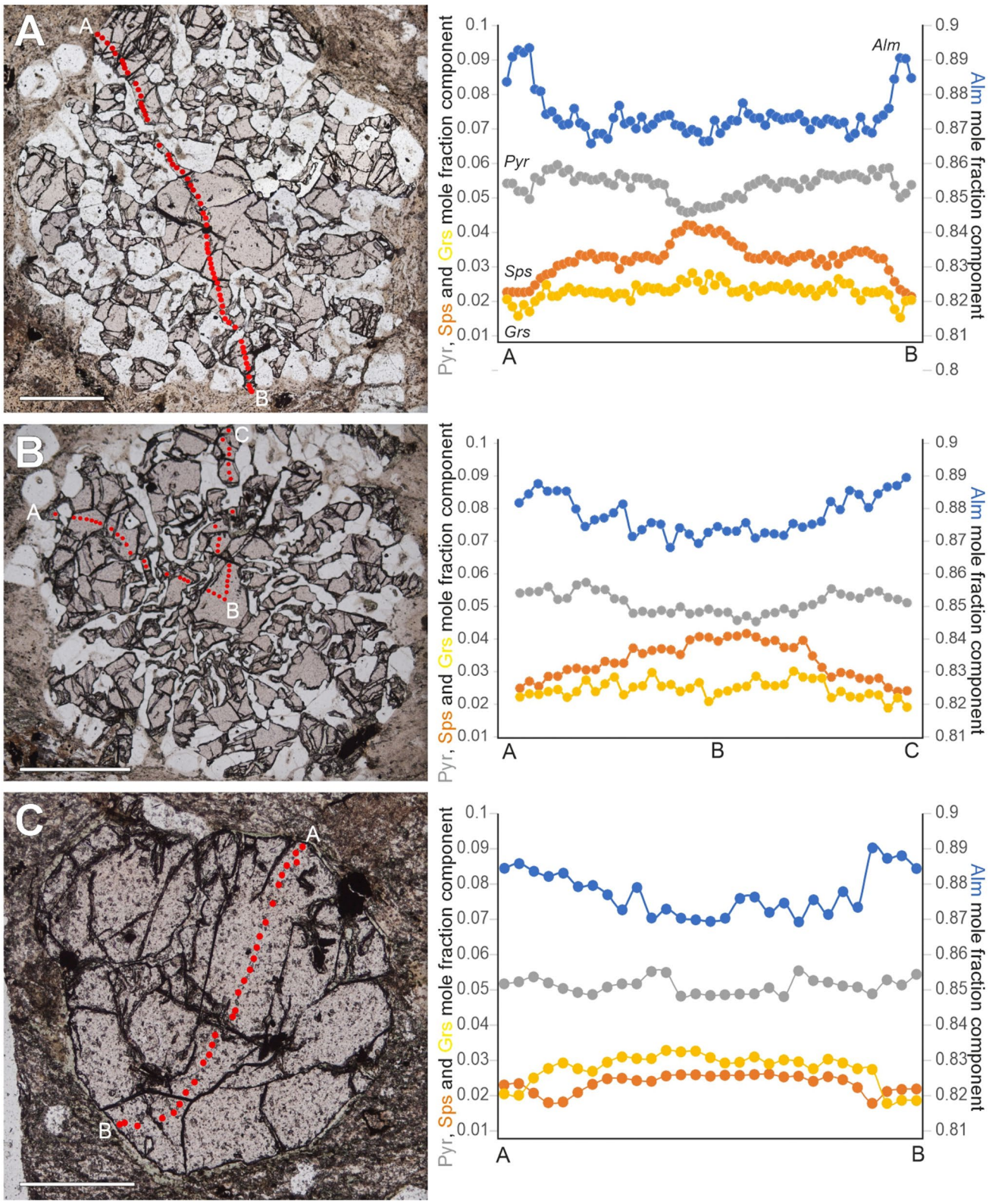

Fig. 6 **A**–**C** Representative rim-to-rim EPMA major element profiles of two garnets intergrown with quartz and one smaller euhedral garnet. Scale bars are 400 µm

and comparatively higher X_{Grs} (Fig. 6C). Euhedral garnets often exhibit no major element zoning, although larger sized crystals display some major element chemistry zoning, with Ca- and Mn-enriched ($X_{Grs} > X_{Sps}$) cores and slight rimward increases in Mg and Fe (Fig. 6C). Both garnet types occasionally show the presence of thin retrograde rims in contact with the groundmass, with small increases in Mn and Mg and similar decreases in Fe (Fig. 6C).

The mapped garnet intergrown with quartz (Fig. 7) shows a decrease in Mn toward the rim and a small increase in the mantle area. Furthermore, there is prominent concentric trace element zoning, characterized by the presence of an inner core enriched in V, Sc, HREE, Zr and Ti, and an outer core marked by a sharp decrease in trace element concentrations (Fig. 7). Both core domains have well-developed oscillatory zoning, as best displayed in the V and HREE maps (Fig. 7). The outer core is overgrown by a trace element-enriched mantle (HREE, Sc, V, Ti and Zr), with marked oscillatory zoning, and rimward trace element decreases (Fig. 7). The trace element-rich mantle is broader in size in the HREE, Sc and V maps, whereas the Zr and Ti maps display a thinner mantle (Fig. 7), although these differences can also be related to the thickness of the oscillatory zoning. Furthermore, the outer core–mantle transition seems to coincide with the appearance of filmy, lobate quartz intergrowths, but there is no evidence of dissolution between the core–mantle and mantle–rim domains. Also noticeable in some EPMA profiles in Fig. 6, the mantle area shows a slight increase in Mn (Fig. 7) and Ca (ESM3).

Garnets intergrown with quartz display a wide range in Y (167–3250 µg/g), P (119–733 µg/g), ∑REE (133–1773 µg/g) and ∑HREE (121–1758 µg/g), whereas smaller euhedral garnets have markedly lower trace element concentrations (Y 171–1486 µg/g, P 186–383 µg/g, ∑REE 133–1136 µg/g and ∑HREE 121–856 µg/g). Ti concentrations varies from 152 to 1870 µg/g in garnet intergrown with quartz, and 408 to 1061 µg/g for euhedral garnets, while Zr and Hf concentrations are overall similar in both euhedral garnets and garnets intergrown with quartz (20–260 µg/g and 30–250 µg/g, respectively). Chondrite-normalized REE patterns of all garnet analyses show strong LREE depletion and M-HREE enrichment, variably pronounced Eu anomalies (Eu/Eu* between 0.02 and 0.07) and highly variable Lu_N/Gd_N ratios (Fig. 8). Garnet intergrown with quartz shows wider ranges in the Lu_N/Gd_N ratios (from 0.03–8.09) than the euhedral quartz-free garnet (0.06–0.73) (Fig. 8). LA-ICP-MS trace element profiles from other garnet–quartz intergrowths show Y + HREE rich cores and a variably trace element enriched mantle, with sharp decreases in trace element concentrations between both domains (ESM3). This zoning is particularly noticeable in Y, Lu and Yb in all the garnet transects, whereas MREE, Ti, Zr, P and Hf display wide variations in the core and mantle zones (ESM3). A trace element profile (rim-to-rim) of a euhedral garnet shows the presence of an inner core with high Zr, Ti, Hf, P and MREE, and low HREE + Y (Fig. 8). The sharp decrease in Zr, Ti and MREE in the outer core area coincides with increases in Y, Yb and Lu, whereas Y and HREE decrease toward the rim with the trace element profile showing a second mantle enrichment in Zr, Ti, MREE and P (Fig. 8).

Whole-rock geochemistry

Major and trace element compositions of the garnet-bearing volcanic rocks are presented in ESM2 Table 3 and methods are in ESM4 (Fig. 9). All samples show moderate to high SiO_2 contents (67.2–80.1 wt%), with A/CNK > 1, mostly above 1.1. Most major elements and Zr define scattered and broad negative correlations with increasing SiO_2 (Fig. 9; ESM2 Table 3). $FeO_T + MgO$ (maficity), Al_2O_3 and TiO_2 as well as Eu, U and Zr show quasi-linear negative correlations with SiO_2 (Fig. 9). A/CNK, TiO_2, Al_2O_3, Mg# define positive trends with increasing $FeO_T + MgO$, as well as Zr, Hf, Yb, Sm and Nb, although with some scatter, whereas CaO and SiO_2 display negative correlations with $FeO_T + MgO$ (Fig. 9).

The garnet-bearing felsic volcanic rocks are also characterized by variable, but overall high total REE concentrations (41–431 µg/g) and markedly negatively sloped C1-normalized REE patterns (La_N/Yb_N from 3.6–33.1). REE patterns have negative LREE and HREE slopes (La_N/Sm_N and Gd_N/Lu_N between 1.13–3.4 and 1.2–5.9), negative Eu anomalies ($Eu/Eu^* = Eu_N/(Sm_N x Gd_N)^{0.5}$) of 0.28 to 0.40 (0.33 average) and mildly positive Ce anomalies (0.92–1.14, avg. 1) (Fig. 10A). Primitive mantle (PM)-normalized trace element diagrams show pronounced enrichments in LILE (e.g., Rb, Ba), Th and U over HSFE (e.g., Nb), with marked negative anomalies in Pb, Sr and Ti (Fig. 10B). Moreover, the garnet-bearing felsic volcanic rocks show low Nb (8–24 µg/g), Ta (0.8–1.6 µg/g) and sub-chondritic Nb/Ta (9–18), low Cr (< 0.5–8.3 µg/g), V (< 5 µg/g), and Ni (2–9 µg/g), and Zr concentrations between 80 and 315 µg/g.

Zircon morphology, geochronology and geochemistry

All dated samples from both drill cores represent different facies of a specific volcanic deposit, as indicated by geological, stratigraphic, and physical volcanology data. Thus, U–Pb zircon data are integrated with geological and stratigraphic data, providing a robust framework with which to interpret the results. Zircon populations were calculated using the Sambridge and Compston (1994) method. All

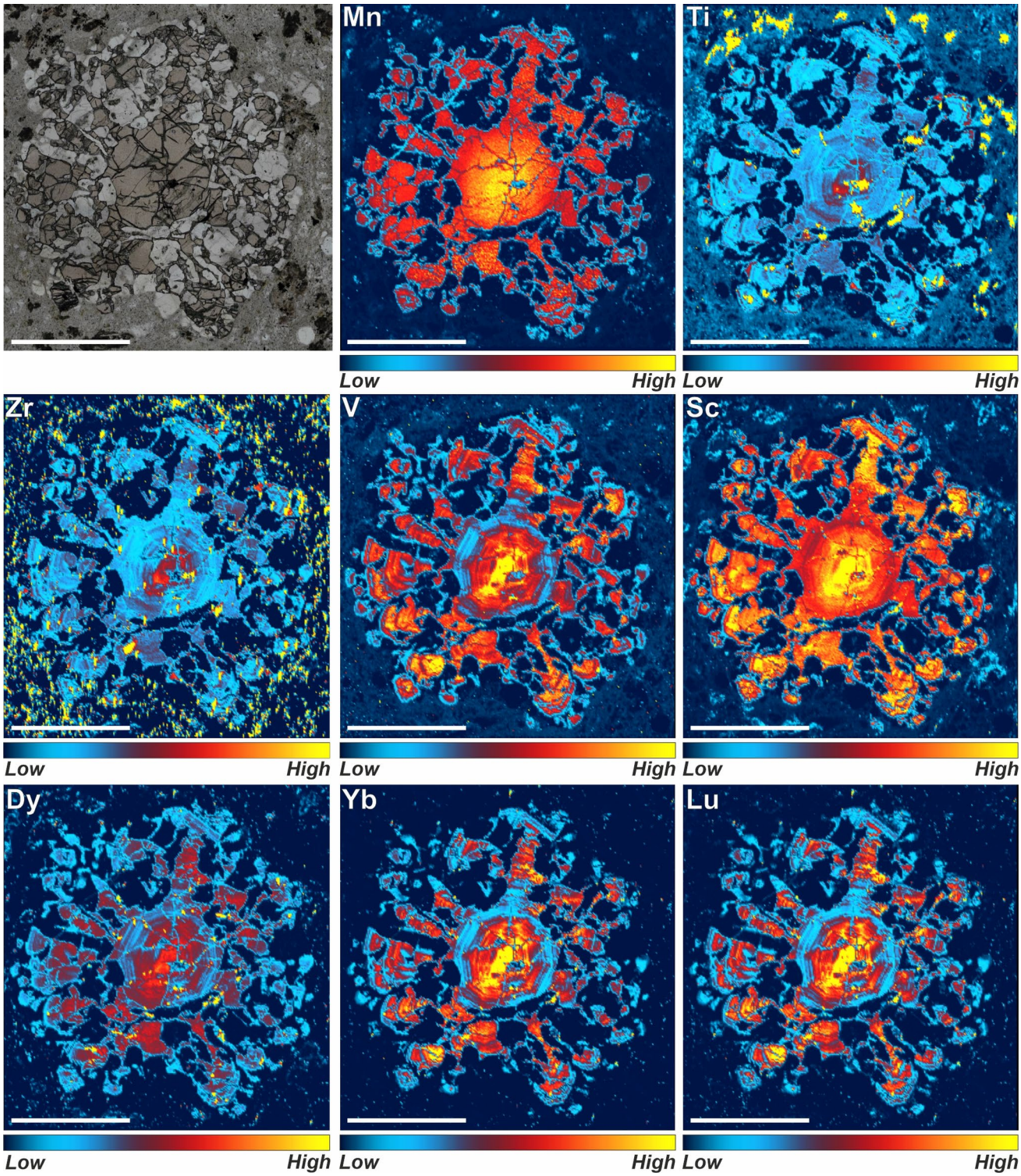

Fig. 7 LA-ICP-MS trace element maps of a garnet intergrown with quartz. Scale bars are 400 µm. Additional maps of Ca, Ce, Gd and Dy and trace element spot analyses profiles of garnet–quartz intergrowths are provided in ESM3

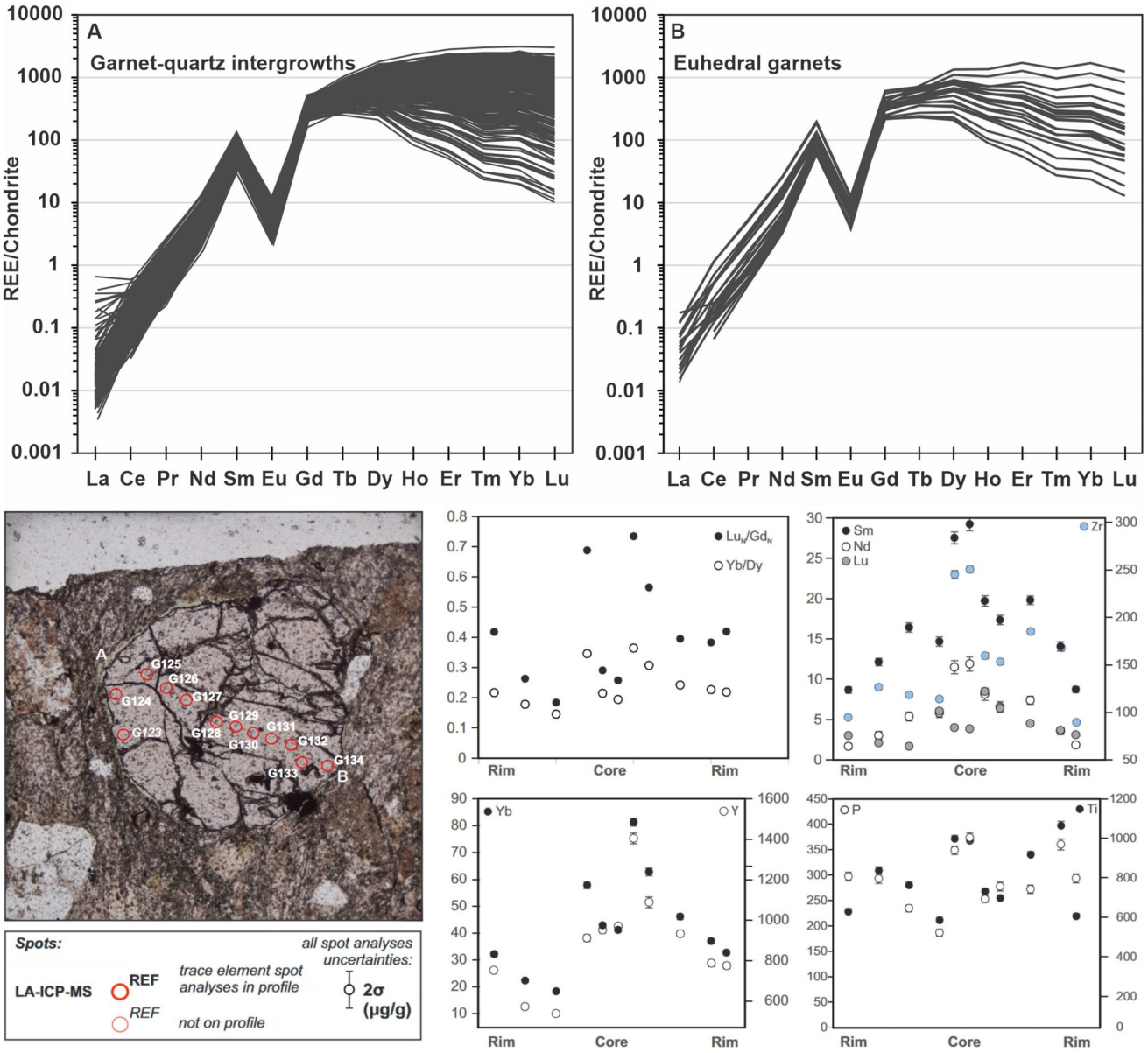

Fig. 8 **A** and **B** Chondrite-normalized garnet REE data [values from McDonough and Sun 1995); **C** Trace element (Zr, REE, Y, P and Ti)] variations along a rim-to-rim profile **A**–**B** for a euhedral garnet (major element in Fig. 6)

reported uncertainties for individual analyses and calculated zircon populations are 2σ. Data are provided in ESM2 Table 5 and 6 and detailed methods are provided in ESM4.

SHRIMP U–Pb zircon geochronology

Zircon from the four CT-01 drill core samples comprise small (< 200 µm in length) euhedral to subhedral grains or fragments, and are transparent, prismatic, and elongated (from 2:1 to 4:1 length/width ratios). All the grains show homogeneous textures, fractures and the presence of inclusions in BSE images. Cathodoluminescence (CL) images show some variation of CL response and the common presence of typical magmatic textural features (as in Corfu et al. 2003) such as oscillatory zoning and sector zoning, and in some grains a homogeneous CL response (ESM1). Most grains are characterized by similar morphologies, with well-developed {211} pyramids, dominating over {101}, and dominant {110} prisms over {100}. There is no relationship between specific textural features or CL response to any of the individual zircon populations. One important feature is the lack of overgrowths and texturally complex zircons.

Zircon U–Pb dates from all four samples (CT-01 drill-core) display a wide range of concordant dates (Fig. 11A,

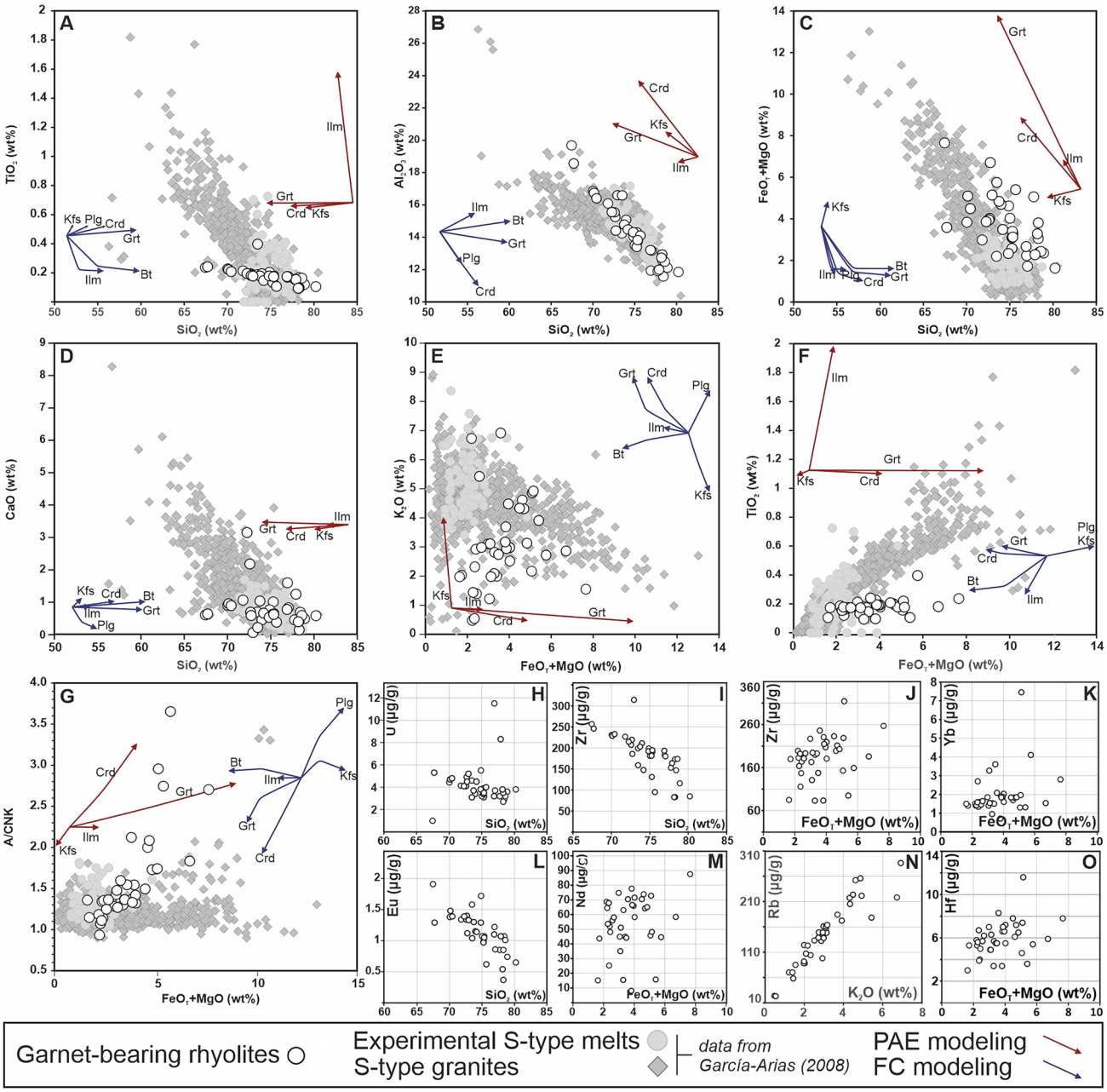

Fig. 9 **A** to **G** Major element Harker plots for the Cotovio garnet-bearing rhyolites (recalculated to a volatile-free basis). **A** TiO_2; **B** Al_2O_3; **C** FeO_T+MgO; **D** CaO. **E** K_2O *vs* FeO_T+MgO; **F** TiO2 vs FeO_T+MgO; **G** A/CNK vs FeO_T+MgO; **H** U vs SiO_2; **I** Zr vs SiO_2; **J** Zr vs FeO_T+MgO; **K** Yb vs FeO_T+MgO; **L** Eu vs SiO_2; **M** Nd vs FeO_T+MgO; **N** Rb vs K_2O; **O** Hf vs FeO_T+MgO. Additional information on peritectic assemblage entrainment (PAE) and fractional crystallization (FC) modeling are provided in ESM2 Table 4. Plots **A**–**G** show also the vectors calculated for peritectic phase entrainment (in red), of garnet, cordierite, K-feldspar (20%) and ilmenite (2%), and fractional crystallization (in blue) of plagioclase, K-feldspar, biotite, garnet and cordierite (10%), and ilmenite (2%)

C), suggesting the presence of multiple zircon populations. The older $^{206}Pb/^{238}U$ dates ($n=4$), from all samples, scatter between *ca.* 470 ± 12 Ma up to *ca.* 439 Ma, with variable Th/U ratios (0.12–1.98; Fig. 11E), whereas the remaining $^{206}Pb/^{238}U$ dates ($n=47$, from all samples) range from *ca.* 400 Ma up to *ca.* 351 Ma. The analyses define four main zircon populations at 453 ± 6 Ma, 407 ± 5 Ma, 384 ± 6 Ma, and 365 ± 1.6 Ma (Fig. 11A), with Th/U ratios between 2.01 and 0.11 (Fig. 11E).

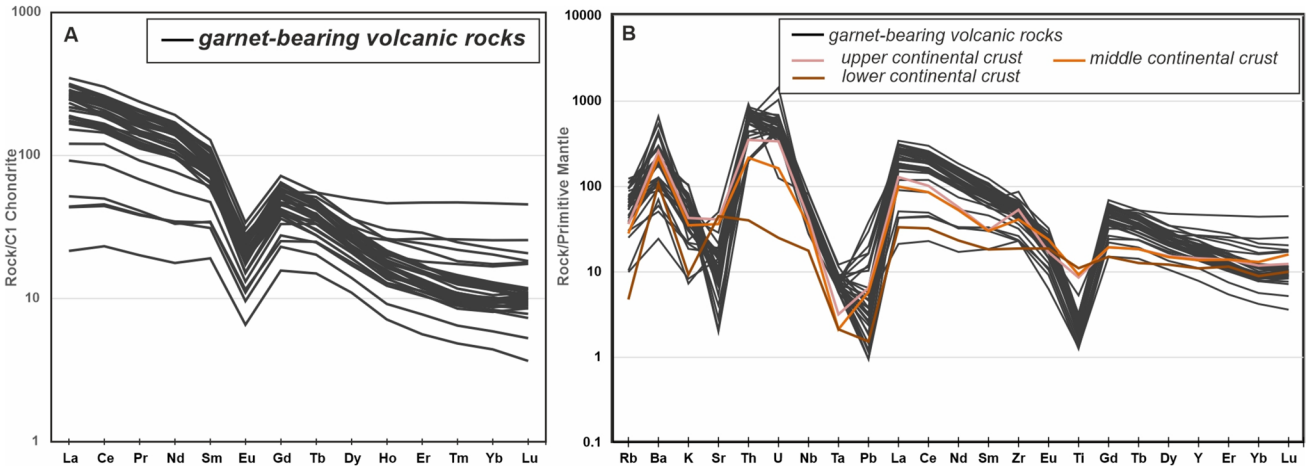

Fig. 10 **A** C1 Chondrite-normalized REE (values from McDonough and Sun 1995); **B** PM-normalized (values from Palme and O'Neill 2014) trace element plot of the garnet-bearing rhyolites whole-rock samples

LA-ICP-MS U–Pb zircon geochronology

Zircon grains from the four LA-ICP-MS dated samples of the CT08001 drill core are small (< 200 µm in length). The euhedral zircon grains and zircon fragments with length–width ratio of 2:1 to 4:1. Common CL textures include oscillatory zoning or a homogeneous CL response. Zircons also show well-developed {211} pyramids and {110} prisms, dominating over {101} pyramids and {100} prisms.

The zircon LA-ICP-MS U–Pb data of all four samples also show a wide variation in concordant $^{206}Pb/^{238}U$ dates ($n = 104$ analyses within 10% concordance) spanning in a multi-peak age spectrum (Fig. 11B). The youngest dates ($n = 69$, from all samples) range from 338 ± 4 up to 378 ± 6 Ma, and comprise most of the data. They define four major peaks at 345 ± 1 Ma, 359 ± 1 Ma, 366 ± 1 Ma, and 374 ± 1 Ma. These overlap with the main volcanic episodes in the stratigraphy in Neves-Corvo (Fig. 11B), whereas the remaining older $^{206}Pb/^{238}U$ dates ($n = 35$, from all samples) range from 387 ± 6 and 453 ± 6 Ma, defining several minor peaks between 390 and 400 Ma (Fig. 11B).

Zircon trace element geochemistry

The LA-ICP-MS zircon trace element data is presented in ESM2 Table 7 and the analytical methods in ESM4. The zircon crystals from all individualized populations display coherent REE patterns (Fig. 12A), characterized by strong MREE and HREE enrichment, variable MREE–HREE segments (Yb_N/Dy_N between 0.68 and 6.65), low Gd_N/Yb_N (0.03–0.67) and ∑LREE (0.44–47.78 µg/g), and variable negative Eu and positive Ce anomalies (0.02–0.7 and 0.83–4.89, respectively; Fig. 12). Noticeably, a few zircon analyses with ages from *ca.* 350–370 Ma (defining a *ca.* 365 Ma main population) display lower Gd_N/Yb_N values and flat REE patterns (Fig. 12A).Other trace element compositional ranges of the zircon populations are also similar, with variable Hf (9560–15100 µg/g), Y (1079–11400 µg/g), Ti (3.42–34.2 µg/g, two outliers of 59 and 72 µg/g) concentrations (Fig. 12B–E). The majority of the zircon grains show LREE-I values (Dy/Nd + Dy/Sm) above 10, indicating no significant post-crystallization alteration (Bell et al. 2019). Ti is positively correlated with Th/U (Fig. 12D), and negatively correlated with Hf (Fig. 12F), the latter suggesting decreasing temperatures with magmatic differentiation. Hf also displays a positive correlation with Y (Fig. 12E), and the data appear to define two main trends, one with higher Y (above 9000 µg/g) and one with lower (up to 6000 µg/g) Y contents. Additionally, Y shows a broad and scattered negative correlation with Ti, also displaying two main compositional trends (Fig. 12H). Furthermore, Y is positively correlated with Gd/Yb ratios. Eu anomalies show a positive correlation with Hf (Fig. 12G). The overall low positive Ce/Ce* values suggest crystallization under reducing conditions, due to the higher compatibility of tetravalent Ce in relation to Ce^{3+}. Oxygen fugacity estimates, calculated using the zircon oxybarometer of Loucks et al. (2020) yield similar fO_2 estimates for all zircon analyses, mostly under reducing melt conditions and ΔFMQ values between 1.1 and –5.6. The average fO_2 of the *ca.* 365 Ma zircon population is -16.7 ± 2.1 (ESM3 Table 7). (Fig. 12, I, J). These results, although rather low, are within the range of fO_2 estimates for other reduced granites and silicic volcanic rocks (e.g., Pichavant et al. 1988, 2024; Bucholz et al. 2018; Zhu et al.

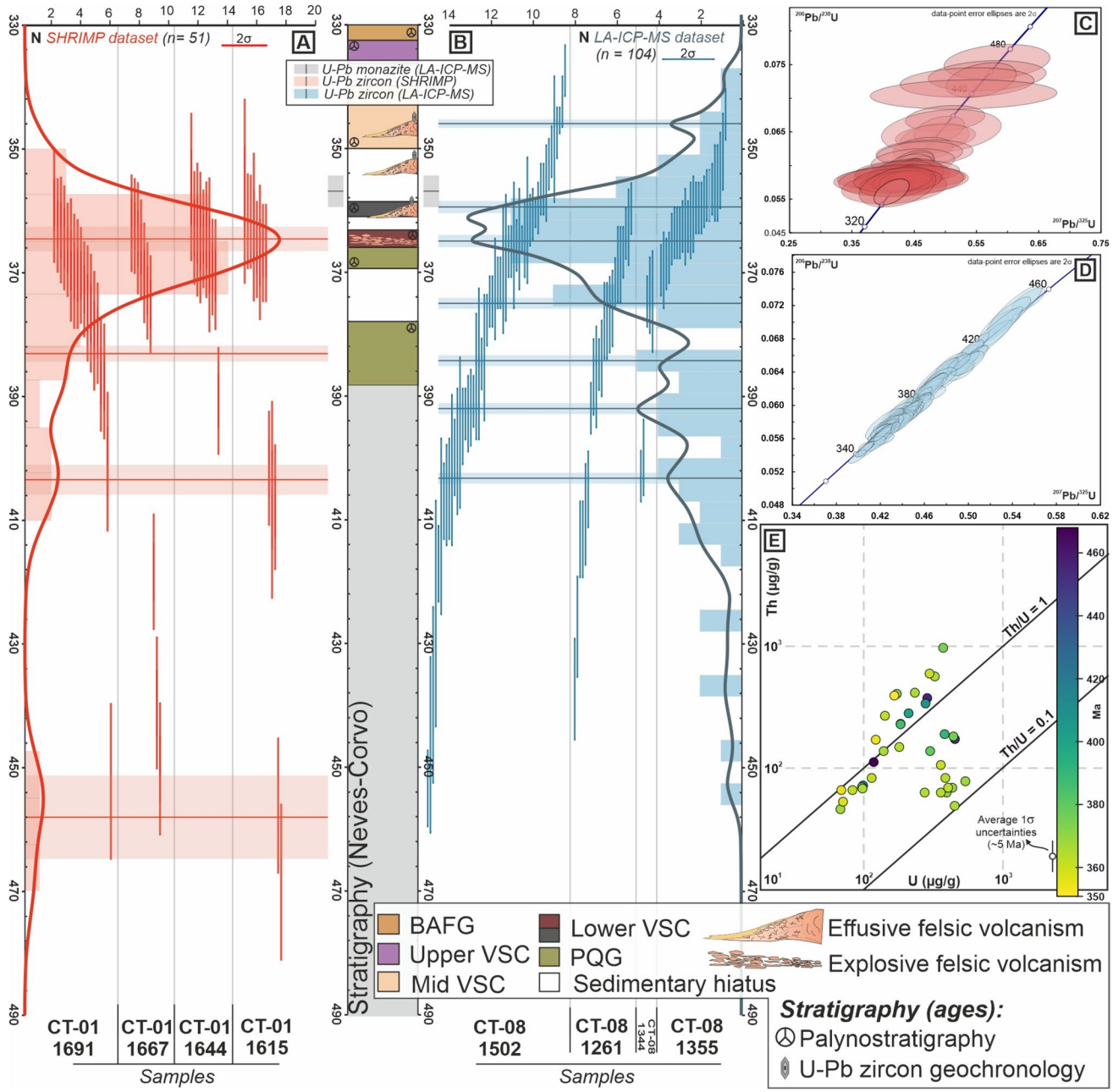

Fig. 11 **A** and **B** Probability density functions for the SHRIMP and LA-ICP-MS geochronology datasets with ranked U–Pb SHRIMP $^{206}U/^{238}Pb$ dates of the garnet-bearing felsic volcanic rocks; box heights are 2σ. Uncertainties in the individualized zircon populations ages are calculated at the 95% (2σ) confidence level; **C** and **D** Concordia diagrams of the SHRIMP and LA-ICP-MS datasets; **E** Th vs U plot of the SHRIMP zircon analyses

2021; Li et al. 2021; Bell and Kirkpatrick 2021; Nazari-Dehkordi and Robb 2022; Sun et al. 2023; Huang et al. 2023; Vogt et al. 2023; Manor et al. 2023). Furthermore, there is a general trend of increasing ΔFMQ with Eu/Eu* (Fig. 12F), suggesting the role of additional processes in controlling the Eu anomalies besides plagioclase fractionation (Holder et al. 2020; Bell and Kirkpatrick 2021).

Monazite geochemistry and in situ geochronology

Monazite geochemistry

Monazite EPMA data is presented in ESM2 and analytical methods in ESM4. There are four different monazite textural types with distinct compositions: (i) euhedral to

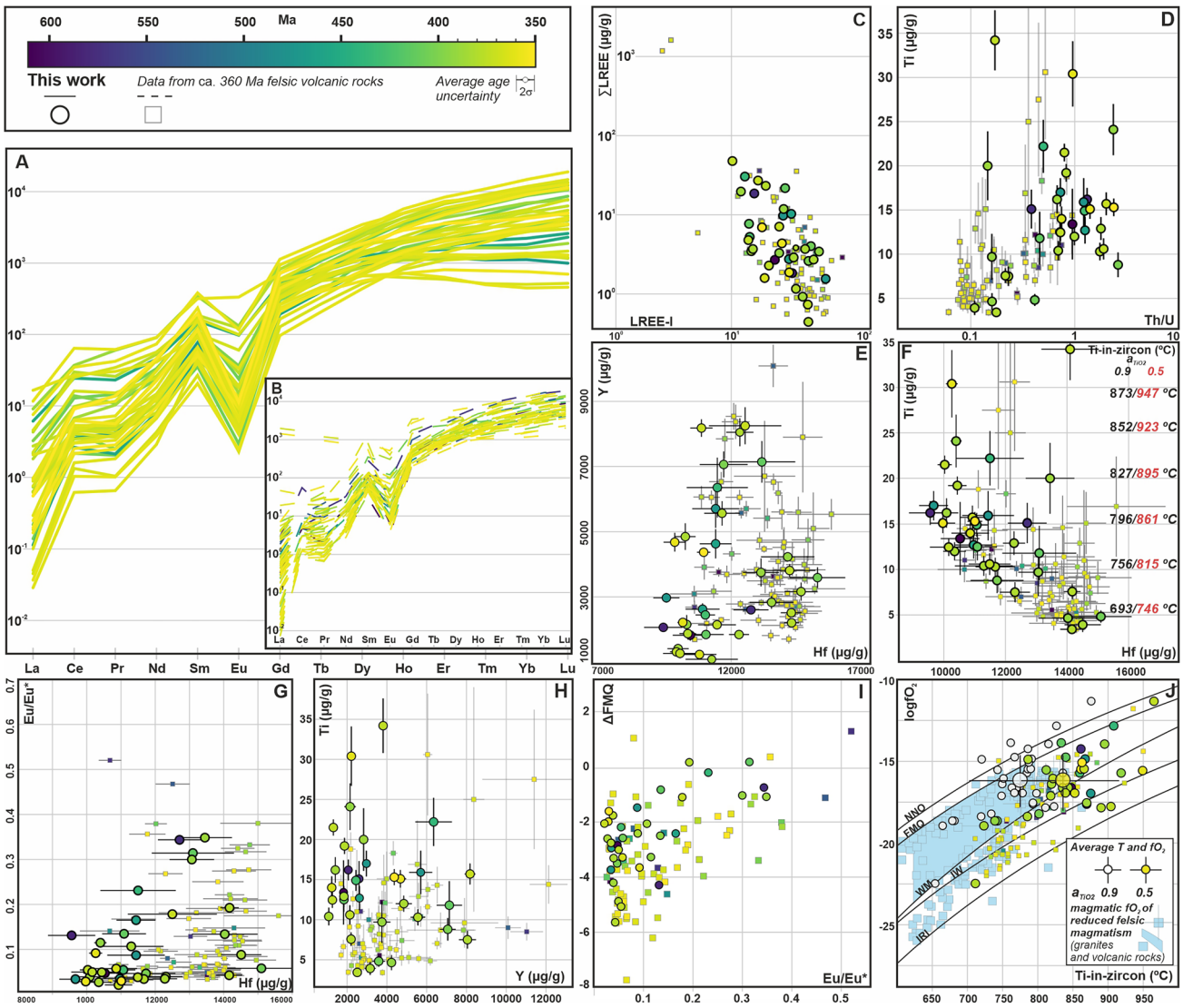

Fig. 12 Zircon trace element geochemistry **A** and **B** Chondrite C1-normalized (from McDonough and Sun 1995) zircon REE patterns; **C** LREE-I vs ∑LREE; **D** Ti vs Th/U; **E** Y vs Hf; **F** Ti vs Hf; **G** Eu/Eu* vs Hf; **H** Ti vs Y; **I** ΔFMQ vs Eu/Eu*; **J** logfO_2 vs $T_{Ti\text{-}in\text{-}zircon}$ (°C). The plotted Ti-in-zircon and fO_2 average data is from the ca. 365 Ma zircon population (see text for details). Data in blue (**J**) compiled from Li et al. (2021), Yang et al. (2000), Bucholz et al. (2018), Manor et al. (2023), Vogt et al. (2023) and Pichavant et al. (2024)

subhedral inclusions in garnet (Fig. 13A–H); (ii) inclusions in muscovite–chlorite pseudomorphs (Fig. 13I); (iii) inclusions in feldspars (Fig. 13J–K) and (iv) small (< 10 μm) anhedral grains near intense garnet replacements by chlorite and included in feldspars (Fig. 13L–M). All monazite analyses show X_{Mnz}-rich compositions (0.88–0.99; ESM2 Table 8), and their geochemical composition is controlled by the huttonite and minor cheralite substitutions (Fig. 13). Euhedral monazite inclusions in garnet and chlorite-muscovite pseudomorphs show variable ∑LREE and Y concentrations (YO_2 from 5.18–1.09 wt%, avg. 2.78 wt%), high Th (ThO_2 > 2.88 wt%) and low Si (apfu) (Fig. 13N–Q). These euhedral monazite inclusions are unzoned in Th and Y, although some grains display some Y and Si variations (Fig. 13N–Q). Euhedral to subhedral inclusions in feldspar display textural and chemical features similar to the euhedral monazite inclusions in garnet and chlorite–muscovite pseudomorphs (Fig. 13N–Q). Anhedral monazite grains (rimming garnet and as feldspar inclusions) show the highest LREE contents, lower Th, and Y concentrations, and variable Si (apfu), up to 0.28 (Fig. 13N–Q).

Monazite U–Pb geochronology

Seventeen LA-ICP-MS U–Pb spots were obtained from four subhedral–euhedral Y- and Th-rich monazite inclusions in

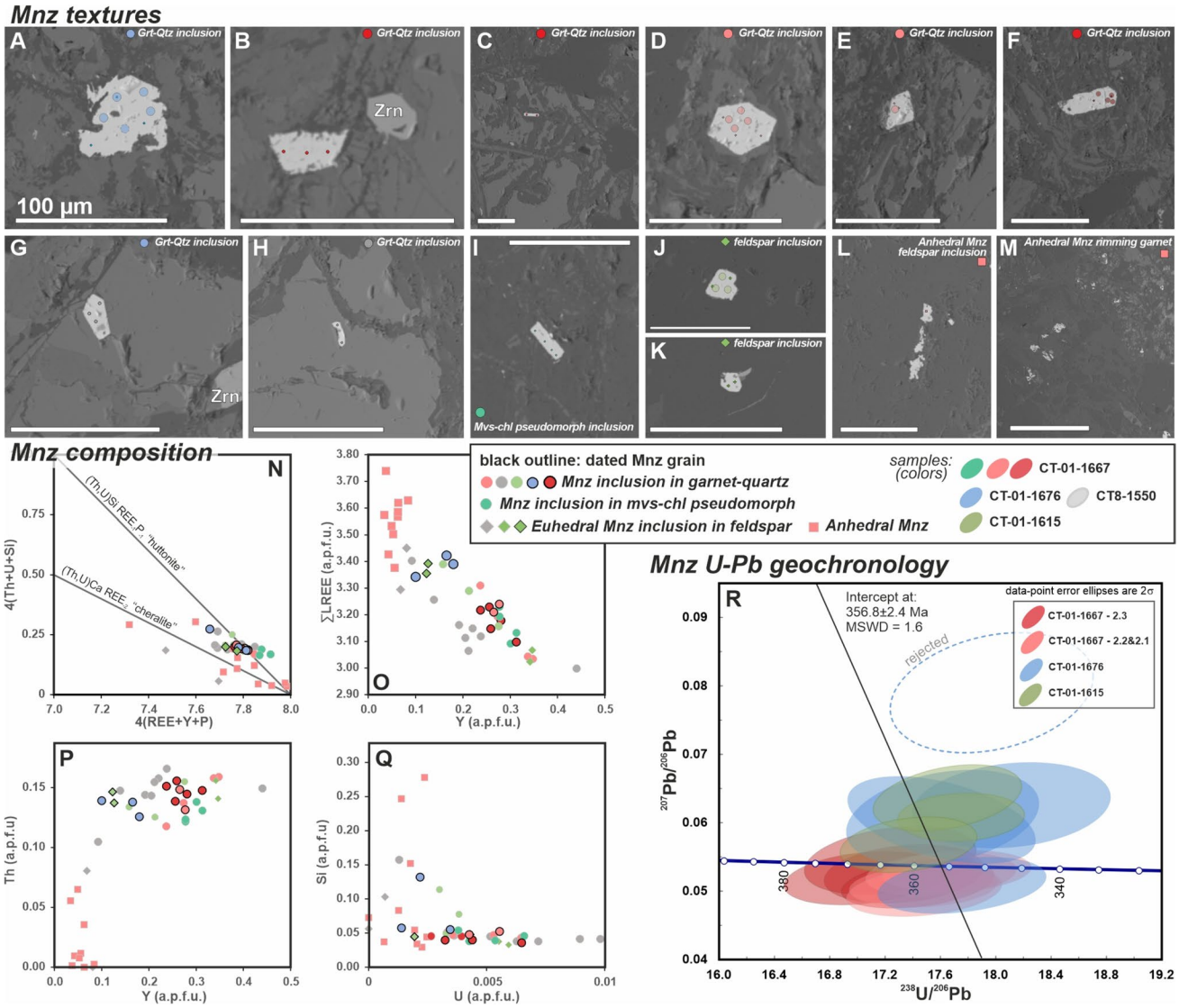

Fig. 13 **A**–**M** Monazite BSE images with EPMA and LA-ICP-MS spot analyses. Scale bars are 100 µm; **N**–**Q** EPMA monazite chemical composition; **R** Tera–Wasserburg concordia diagram of the LA-ICP-MS U–Pb monazite results

garnet intergrown with quartz and one Th-rich euhedral monazite inclusion in feldspar (Fig. 13A, D, E, F, J; ESM2 Table 9; methods in ESM4). One highly discordant analysis (> 10%) was rejected from the dataset (Fig. 13A, R). The remaining sixteen analyses are below 10% discordance, suggesting low common Pb contents. The $^{206}Pb/^{238}U$ data define a Tera–Wasserburg lower intercept age of 356.8 ± 2.4 Ma (MSWD = 1.6; Fig. 13R), anchored at 0.859 ± 0.02, derived from the Stacey and Kramers (1975) terrestrial Pb evolution model. This date overlaps, within uncertainty with the youngest zircon dates from the *ca.* 365 Ma major population of the SHRIMP dataset, and significantly overlaps with the *ca.* 360 Ma age main zircon population in the LA-ICP-MS dataset (Fig. 11).

Geothermobarometric constraints

Ti-in-zircon and zircon saturation temperatures

The reduced zircon fO_2 estimates preclude rutile crystallization ($aTiO_2 = 1$), which is a typical feature of oxidized melts (e.g., Schiller and Finger 2019). This strongly suggests that $aTiO_2$ should be below 1. Independent $aTiO_2$ estimates are not available, especially due to the widespread alteration of primary oxide phases into rutile + titanite + chlorite, possibly resulting from the low-grade metamorphic recrystallization of ilmenite (e.g., Luvizotto et al. 2009; Angiboust and Harlov 2017). Such sub-solidus alteration is also supported by the widespread

porous feldspar textures, and replacement of euhedral albite feldspars by epidote and muscovite (e.g., Plümper and Putnis 2009), hindering the use of oxide phases to estimate magmatic $aTiO_2$ values. Ilmenite-stable silicic melts have variable $aTiO_2$, ranging from at least 0.3 up to 0.9 (Teixeira et al. 2024), although typically considered between 0.4 and 0.5 (Schiller and Finger 2019). Furthermore, variations in $aTiO_2$ are expected during the cooling and evolution of felsic melts, and thus the use of a fixed $aTiO_2$ may also introduce significant discrepancies in the calculated Ti-in-zircon temperatures (Teixeira et al. 2024). As such, we calculate zircon crystallization temperatures using the Ti-in-zircon calibration of Ferry and Watson (2007), excluding two analysis with anomalously high Ti concentrations (59 and 72 µg/g), and considering $aSiO_2 = 1$ and $aTiO_2$ at 0.5 and 0.9. Calculated temperatures with $aTiO_2$ of 0.5 are high and range from 710 up to 965 °C (Fig. 12F, J), whereas those obtained considering $aTiO_2$ of 0.9 are lower, and range between ca. 660 and 890 ºC. Furthermore, the average temperatures of the *ca.* 365 Ma population is 837 ± 66ºC (aTiO2 of 0.5) and 774 ± 60ºC (aTiO2 of 0.9) (Fig. 12J). These latter estimates ($aTiO_2$ of 0.9) are thus preferred but are considered as minimum zircon crystallization temperatures (T_{Zirc}).

Experimental work on Zr solubility in felsic melts resulted in the development of zircon saturation models, which enables predicting the temperature at which a melt with a given composition (M factor) saturates in zircon (Watson and Harrison 1983; Boehnke et al. 2013). Most garnet-bearing rhyolites are within the calibrated compositional range of $0.9 < M < 1.9$ ($M = (Na + K + 2Ca)/Al \cdot Si$ in cation proportions), resulting in zircon saturation temperatures ($T_{SatZirc}$) between 696 and 800 ºC, using the Boehnke et al (2013) model. $T_{SatZirc}$ is inversely correlated with SiO_2 and is positively correlated with $FeO_T + MgO$ (ESM2 Table 3), and the most silicic compositions (71.5–78.3 SiO_2 wt%) display $T_{SatZirc}$ between 696 and 772 ºC (ESM2 Table 3). The presence of inherited zircon implies that the melts were zircon oversaturated or near saturation. As such, the $T_{SatZirc}$ are considered as maximum temperatures of the melts. $T_{SatZirc}$ values overlap with most of the minimum zircon crystallization temperatures (T_{Zirc}).

TitaniQ: Ti-in-quartz

Quartz intergrown with garnet shows a bright and homogeneous CL response and exhibits rounded and smooth-walled embayments (Fig. 14A–D). Five LA-ICP-MS analyses of quartz intergrown with garnet show Ti contents between 92 and 108 µg/g (Fig. 14A–D; ESM2 Table 11). Ti incorporation into the quartz lattice is sensitive to temperature, pressure, melt composition and $aTiO_2$ (e.g., Wark and Watson 2006; Osborne et al. 2022). We use the Ti-in-quartz calibration of Osborne et al. (2022) to model the effects of varying P–T–$aTiO_2$ conditions (Fig. 14E). Quartz crystallization in equilibrium with rutile ($aTiO_2 = 1$) is only shown for comparison, as zircon oxybarometry indicates reduced magmatic fO_2 conditions. The average minimum Ti-in-zircon temperature estimates ($aTiO_2 = 0.9$) are typically lower than those required for dehydration

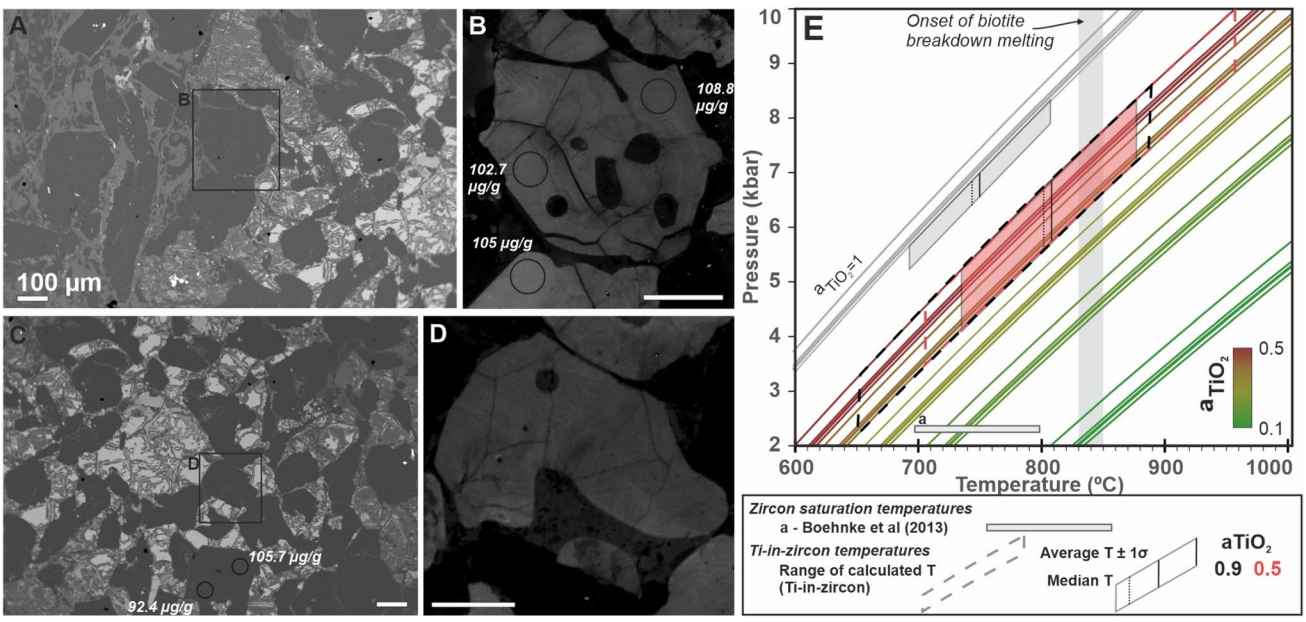

Fig. 14 **A**–**D** BSE and cathodoluminescence (CL) features of the analyzed quartz intergrown with garnet; **E** P-T-aTiO2 results of the analyzed quartz intergrown with garnet

melting involving biotite (> 820–850 °C), although the highest calculated T_{Zirc} for the 350–370 Ma zircon analyses are compatible with dehydration melting involving biotite (up to 870 °C). Considering these high-temperatures and high $aTiO_2$ values (0.9), quartz crystallization is calculated at high pressure conditions (8–10 kbar), whereas a lower $aTiO_2$ of between 0.3 and 0.5 during quartz crystallization results in lower pressure estimates, between 6 and 7 kbar (Fig. 14E). This large range in potential pressure conditions further highlights the importance of constraining $aTiO_2$. The amount of TiO_2 in a melt ($aTiO_2$), however, is not constant in natural systems (Schiller and Finger 2019; Teixeira et al. 2024). $aTiO_2$ in felsic melts may either increase during cooling and crystallization of Ti-poor minerals or decrease due to crystallization and efficient removal of Ti–rich phases. As such, it is likely that different $aTiO_2$ values should be considered when using the Ti-in-quartz and Ti-in-zircon geothermometry (Teixeira et al. 2024).

Discussion

Garnets in silicic volcanic rocks: origin and growth

Origin of the garnets

While more common in low- to high-grade metamorphic rocks, garnet also occasionally occurs as a rock-forming phase in felsic volcanic (Harangi et al. 2002; Lucci et al. 2018; Sieck et al. 2019) and plutonic rocks (Dahlquist et al. 2007; Villaros et al. 2009a; Dorais and Tubrett 2012; Dorais and Spencer 2014; Narduzzi et al. 2017), and in highly differentiated and pegmatitic felsic rocks (Zhang et al. 2001; Breiter et al. 2005; Samadi et al. 2014). Interpretations on the origin of garnets in felsic volcanic and plutonic rocks range from: (i) xenocrystic garnets, derived from the incomplete assimilation of the protolith or other metamorphic country rocks (e.g., Clarke 2007; Scallion et al. 2011); (ii) a peritectic origin, generated during incongruent partial melting reactions and entrained into the extracted melt (Erdmann et al. 2009; Villaros et al. 2009a; Taylor and Stevens 2010; Dorais and Tubrett 2012; Jung et al. 2022); (iii) a phenocryst/liquidus phase, directly crystallizing from the felsic melt (e.g., Lucci et al. 2018; Sieck et al. 2019; Devoir et al. 2021), including in highly fractionated felsic melts or pegmatites (e.g., Samadi et al. 2014; Maner et al. 2019). Textural, major- and trace element data of these phases provide critical insights into the petrogenesis of the host rocks (Clarke 2007; Erdmann et al. 2009; Dorais and Campbell 2022).

Comparing the major element chemistry from garnets of this study with those compiled in Schönig et al. (2021), the garnets from this study overlap with compositions of those from felsic igneous rocks and metamorphic rocks in metasediments (ESM3), which are characterized by low Ca and Mn contents (ESM3). Furthermore, metamorphic garnets are commonly characterized by a variety of metamorphic mineral inclusions, usually display textural evidence of deformation and/or metamorphic mineral growth (e.g., snowball structures), and significant major element core-to-rim compositional zoning (e.g., Groppo et al. 2012). Xenocrystic garnets in felsic plutonic and volcanic rocks also frequently show an association with partially disaggregated and assimilated crustal material (Scallion et al. 2011) or show textural and chemical features that indicate significant resorption, replacement or chemical exchange with felsic melts (Clarke 2007; Devoir et al. 2021). The absence of metamorphic mineral inclusions and of pronounced major element core-to-rim zonation and the lack of other xenolithic material strongly argues an origin of the garnets related to assimilated metamorphic country rocks.

Garnets that crystallize from evolved felsic melts sometimes exhibit similar textural features such as quartz intergrowths and rounded- or lobate-shaped inclusions and graphic-like intergrowths (e.g., Zhang et al. 2001; Breiter et al. 2005; Samadi et al. 2014). Despite the textural similarities, these garnets display strong enrichments in Mn and typically X_{Sps} dominates over other components. The role of Mn in stabilizing garnet at lower pressures has been widely documented, enabling magmatic and metamorphic crystallization at low pressures (< 5 kbar) in the upper crust (e.g., Green 1977; White et al. 2014b). The overall low X_{Sps} contents (X_{Sps} < 4%) of the garnets strongly argues against garnet crystallization during emplacement and melt evolution in a shallow crustal magmatic reservoir (Lucci et al. 2018; Sieck et al. 2019; Devoir et al. 2021), consistent with our Ti-in-quartz pressure constraints that indicate crystallization between 6 and 7 kbar, in the middle–lower crust (Fig. 14).

The textural features of the garnet–quartz intergrowths strongly suggests crystallization in the presence of melt. The abundant quartz inclusions and intergrowths and amalgamated garnet–quartz grains closely resemble those found in granulite-facies migmatites (White et al. 2004; Taylor and Stevens 2010; Taylor et al. 2010; Ferrero et al. 2012; Yakymchuk et al. 2015; Blereau et al. 2017; Goncalves et al. 2021), and also quartz–garnet intergrowths formed during fluid-absent partial melting experiments of biotite-bearing metapelites (Vielzeuf and Montel 1994; Waters 2001; Barbey 2007). Similar peritectic phases and quartz intergrowths can also be found in amphibolite-facies anatectic terranes (Dyck et al. 2019), where fluid-absent muscovite breakdown reactions form peritectic K-feldspar and sillimanite. Film-like, rounded to lobate quartz inclusions and intergrowths are common in peritectic phases, generated during sluggish, kinetically

controlled partial melting reactions under disequilibrium conditions (Waters 2001; Barbey 2007). Quartz intergrown with garnet partially exhibits optical continuity within the garnet–quartz aggregates, but the variable shapes of the quartz intergrowths and inclusions (from film-like and lobate to euhedral inclusions) may also suggest variable effects of post-crystallization shape change and maturation processes (Cesare et al. 2021). However, the CL images of quartz inclusions in garnet show the presence of disequilibrium textural features such as embayments, consistent with rapid quartz crystallization during peritectic garnet growth (e.g., Barbee et al. 2020). The above observations show the garnets are unambiguously of peritectic origin, entrained during melt extraction from the partial melting region.

Despite ample evidence that garnet does not typically survive melt extraction and upper-crustal emplacement and/or eruption due to rapid dissolution–reprecipitation and/or compositional homogenization (Clemens et al. 1997; Villaros et al. 2009a; Taylor and Stevens 2010; Devoir et al. 2021; Jung et al. 2022), our results suggest that diffusion was responsible for major element homogenization of garnet, instead of dissolution–reprecipitation processes. This is further supported by the lack of textural and chemical evidences of dissolution–reprecipitation processes, indicating that peritectic garnets preserve their chemical and textural features. This evidence suggests little interaction and/or re-equilibration of the peritectic garnets with the melt. This may be due to equilibrium with the melt or sluggish diffusivities at the garnet–melt interface, inhibiting dissolution–reprecipitation reactions (Acosta-Vigil et al. 2017), or that the peritectic phases and silicic melt were rapidly extracted from the source region. Indeed, rapid melt loss from the source is required to preserve the anhydrous high-temperature peritectic phases, as melt crystallization and cooling would result in significant garnet back-reaction and replacement (White and Powell 2002; Clemens and Stevens 2016). These processes require the existence of an interconnected melt network in the protolith, which may form at low melt fractions (below 7%; Clemens and Stevens 2016) and possibly enhanced by deformation, ensuring that during the melting reactions the entrained peritectic products are preserved, and transported along with the generated melt.

Trace element zoning and peritectic garnet growth

The trace element LA-ICP-MS spot analyses profiles from garnet-quart intergrowths are broadly consistent with the zoning pattern shown in the mapped garnet grain. However, the smaller (sub)euhedral garnet grains display somewhat distinct trace element distributions, showing an HREE and Y-poor core (Fig. 8), in contrast to the larger garnets intergrown with quartz (Fig. 7). While it can be argued that the garnet transects do not cross the geometric garnet core, the major ($X_{Grs} > X_{Sps}$) and overall lower trace element concentrations of the smaller euhedral garnets suggest these crystallized after the garnet intergrown with quartz. Hence, we interpret the crystallization of the euhedral garnets during partial melting reactions, after the crystallization of the early peritectic garnet–quartz intergrowths.

The oscillatory zoning displayed in the core and mantle mapped garnet intergrown with quartz could have developed during subsolidus metamorphic garnet growth (Konrad-Schmolke et al. 2022). However, there is no textural and/or compositional evidence for the presence of dissolved xenocrystic sub-solidus garnet cores (*e.g.*, Rubatto et al. 2020; Devoir et al. 2021; Jung et al. 2022). The highest estimated minimum zircon crystallization temperatures (> 800 °C) and the presence of Th-Y-rich monazite inclusions in the core, mantle and rim of the peritectic garnet further shows garnet crystallization at high-temperatures and in the presence of a melt and thus under supra-solidus conditions. The pronounced oscillatory zoning in the garnet core, mantle, and rim in most trace element maps is thus interpreted as resulting from the competing effects of trace element incorporation during peritectic garnet crystallization and the supply rate from the melt via diffusion during partial melting. More importantly, the inner core and mantle are similarly enriched in V, Sc, Zr, Ti and HREE and display sharp compositional gradients. Therefore, the mapped zoning should reflect the breakdown of major and accessory phases during partial melting reactions. While V and Sc indicate the breakdown of biotite during melting reactions (Yang and Rivers 2000; Dorais and Tubrett 2012), the HREE, Zr, Ti and Y zoning attest to the dissolution of accessory phases such as zircon, monazite or apatite during partial melting reactions involving biotite (Dorais and Tubrett 2012; Yakymchuk 2017; Rubatto et al. 2020; Johnson et al. 2021).

Garnet-bearing rhyolites: geochemistry, zircon cargo, and source constraints

Geochemical variation of the garnet-bearing rhyolites

There is a clear lack of magma mixing indicators, such as microgranular intermediate-mafic igneous enclaves, resorption, and disequilibrium textures in feldspar and other minerals, besides garnet and pinitized cordierite. The low Mg#, Zr contents and other geochemical features (e.g., the strongly peraluminous character) also attest to magma mixing processes with mafic or intermediate melts as not being a significant process in the generation of the IPB garnet-bearing rhyolites (e.g., Mitjavilla et al. 1997).

The broad positive correlation of K_2O vs $FeO_T + MgO$ is an unusual feature among granitoids and S-type volcanic rocks (Clemens and Stevens 2012) and may indicate a role of

biotite fractionation (Clemens et al. 2017a). However, biotite is scarce in all the samples, and its modal amount is not compatible with significant amounts of biotite fractionation. The positive correlation of K and maficity and the constant K/Rb suggests no fractionation of K-feldspar and overall low K melts, whereas the increase of peraluminosity and Yb with maficity highlights the absence of garnet, cordierite and biotite fractionation (e.g., Champion and Bultitude 2013), in agreement with the fact that garnet and cordierite are peritectic and not liquidus phases. Considering all the plots in Fig. 9, no coherent fractionating assemblage seems capable of reproducing the main major element geochemical trends, and thus, fractional crystallization is ruled out as a main driver of the geochemical variation of the garnet-bearing volcanic rocks.

Recently, several studies have proposed and shown that the geochemical variability of S- and I-type volcanic and plutonic rocks reflects, in some cases, the entrainment of peritectic phases (Stevens et al. 2007; Villaros et al. 2009b; Dorais and Spencer 2014; Clemens et al. 2017b; Bailie et al. 2020; Zhu et al. 2021; Dorais and Campbell 2022). The range in maficity and the positive correlations with A/CNK, TiO_2, Y, Yb, Sm, Zr, Hf, Th, La, Eu and Ce are all hallmarks of PAE. More specifically, the negative correlation of Ca with maficity suggests entrainment of Ca-poor garnet (Stevens et al. 2007), which is similar to the composition of the entrained peritectic garnets in this study. Furthermore, the positive correlation between maficity and A/CNK, K and Y, Yb, Sm and Nd suggests the entrainment of peritectic cordierite, K-feldspar and garnet. The small slope in the Ti vs $FeO_T + MgO$ plot (Fig. 9F) further indicates a small proportion of peritectic ilmenite entrainment, also in accordance with the textural and mineralogical data. Furthermore, the negative anomalies in K and Rb further support the presence of peritectic/residual K-feldspar. The lack of knowledge on the chemical composition of the protolith, the melt it generated and the composition of the peritectic phases other than garnet, means that the modeling presented in Fig. 9 can only provide a semi-quantitative/qualitative approach of the role of PAE. Nevertheless, the geochemical trends defined by the garnet-bearing rhyolites can be satisfactorily reproduced by entrainment of up to 15% of peritectic garnet, cordierite, and K-feldspar, and less than 1% peritectic ilmenite, into a highly silicic melt. The systematic positive correlation of Zr, Hf, La, Ce and zircon saturation temperatures with maficity also highlights the role of zircon and monazite co-entrainment, generated and/or liberated from the breakdown of biotite during melting reactions (e.g., Villaros et al. 2009b), which are common inclusions in the entrained peritectic garnets and pinitized cordierite and also in intergrown quartz and in feldspar crystals. Ilmenite and Ti–rich biotite are the most common residual phases generated during partial melting of metasedimentary rocks (White et al. 2014a) and are often found in high-temperature migmatites. The strongly negative Ti anomalies compared to continental crust, together with the marked Ta and Nb ($Ta < Nb$) anomalies suggest that ilmenite and Ti–rich biotite were residual phases during melting reactions and were not significantly entrained into the extracted melt (Stepanov et al. 2014). The geochemical trends defined by the garnet-bearing rhyolites thus mainly reflect entrainment of peritectic minerals (garnet, cordierite, K-feldspar and minor ilmenite), generated during partial melting reactions involving fluid-absent breakdown of biotite into a highly silicic melt.

Protracted zircon cargo: source area, incremental pluton growth and geochemistry

The zircon U–Pb data from the garnet-bearing rhyolites show a wide range of apparent ages, a common feature of crustal-derived granitic magmas (Villaros et al. 2012; Ferreira et al. 2019; Clemens et al. 2023; Vogt et al. 2023). Furthermore, the U–Pb dates in both the LA-ICP-MS and SHRIMP datasets show significant scatter but define overlapping zircon populations, and are interpreted by integrating the available geological (geochronological, palynological and lithostratigraphic) data.

The youngest zircon population (ca. 345 Ma, only seen in the larger LA-ICP-MS dataset) constrains the eruption age of the felsic volcanic rocks, and agrees with the available palynological and stratigraphic data (mid and upper VSC sediments) estimated at ca. 350–330 Ma (Figs. 3, 11; Oliveira et al. 2004; Carvalho et al. 2017). The main zircon population at *ca.* 365 Ma (which encompass zircon grains with ages from ca. 350 to 370 Ma) overlaps with the age of a major explosive volcanic episode in the Neves-Corvo area (rhyolite fiamme-facies volcanic rocks; Rosa et al. 2008), interbedded with the Corvo formation, dated from ca. 363 to 365 Ma (Oliveira et al. 2004; Pereira et al. 2021). These analyses might also include younger zircon grains which are not analytically distinguishable from the ca. 365 Ma major population due to the individual uncertainties (e.g., Large et al. 2020) dataset. This is further supported by the varying Y/Hf and Y/Ti trends and Gd/Yb ratios of the zircon analyses, some of which display flat REE patterns, suggesting HREE partition into garnet prior to zircon crystallization (e.g., Taylor et al. 2015). The zircon geochemistry dataset also shows that Y is positively correlated with the Gd/Yb ratios, further supporting the role of garnet crystallization in controlling Y-HREE contents of zircon. Additionally, the high Th of the analyzed monazite grains (see discussion below), and positive correlation of zircon Ti with Th/U also suggests that monazite crystallization controlled the Th/U ratios of magmatic zircon (Pineda et al. 2022; Vogt et al. 2023).

In both datasets, the individual zircon populations overlap, within uncertainty, with published zircon U–Pb ages in the Neves-Corvo and Rosário anticline, and also in other sectors of the IPB (Rosa et al. 2009; Albardeiro et al. 2023). The zircon populations inherited from the melt source region (400–414 Ma; 420–440 Ma; 450- 470 Ma) overlap within uncertainty with published zircon U–Pb ages in the Neves-Corvo and Rosário anticline, and also in other sectors of the IPB (Barrie et al. 2002; Rosa et al. 2009; Valenzuela et al. 2011; Lains Amaral et al. 2021; Pereira et al. 2021; de Mello et al. 2022; Albardeiro et al. 2023). The inherited zircon dates also broadly overlap with zircon ages found throughout Avalonia and in the Meguma terranes, especially with Ordovician metasediments from the upper Meguma Supergroup (Murphy and Hamilton 2000; Waldron et al. 2009; Braid et al. 2012; Shellnutt et al. 2019), further supporting a relationship between the peri-Gondwana Meguma terrane and the unexposed SPZ basement (e.g., Braid et al. 2012).

Palynological constraints from the oldest known PQG metasediments places the onset of sedimentation in the IPB to the Middle Devonian (387–384 Ma) (Mendes et al. 2020), which indicates that zircon crystals younger than *ca.* 390 Ma cannot be source-inherited or derived from other country rocks. Instead, the abundant presence of pre-eruption Devonian zircon grains can only be explained by the remobilization and extrusion of previously crystallized felsic melts (e.g., Albardeiro et al. 2023). These younger zircon populations overlap remarkably with major volcanic episodes in the Rosário–Neves-Corvo anticline and in other sectors of the IPB (Fig. 11), namely: *ca.* 360 and 365 Ma in the Neves–Corvo-Rosário region (Rosa et al. 2008; Pereira et al. 2021), and *ca.* 370–376 in the Cercal region (Rosa et al. 2009). Older zircon ages (*ca.* 390–380 Ma) also overlap with previously recognized "xenocrystic" U–Pb zircon ages in felsic volcanic rocks of the IPB (Barrie et al. 2002; Rosa et al. 2009; Valenzuela et al. 2011; Lains Amaral et al. 2021; Pereira et al. 2021; Albardeiro et al. 2023). These medium- to high-temperature reduced felsic melts were thus stored at temperatures below the solidus in an upper-crustal pluton which records the episodic emplacement and crystallization of felsic melts in the upper crust since *ca.* 390 Ma, possibly marking the onset of the intracontinental rifting in the South Portuguese Zone basement.

Evidence for high-temperature partial melting of the middle crust

Peritectic assemblages formed after biotite breakdown reactions are dominated by garnet, cordierite and/or orthopyroxene, depending mainly on the range of pressures and protolith compositions (*e.g.,* Johnson et al. 2021). Therefore, the entrained peritectic garnet and cordierite indicate incongruent melting reactions involving biotite.

While the low X_{Pyr} contents of the entrained peritectic garnets may suggest low-temperature conditions, as Mg in garnet increases with temperature due to the Fe–Mg exchange with biotite, Fe-rich garnet compositions are common in the middle crust, due to Fe–Mg partitioning with coexisting cordierite (Hensen and Green 1972; Holdaway and Lee 1977). Cordierite is a common phase in low-pressure (< 5 kbar) metasedimentary migmatites and S-type granites (Clarke 1995; Barbey et al. 1999; Groppo et al. 2013; White et al. 2014b), but the stability of (Mg-rich) cordierite extends up to 7–8 kbar, in equilibrium with garnet, following the melt-producing reaction: biotite + aluminosilicate + quartz + albite = garnet + cordierite + K-feldspar + melt (Holdaway and Lee 1977; Spear et al. 1999; Vielzeuf and Schmidt 2001), and its stability should be expanded by increasing protolith Mg#. Hence, we interpret the low Mg- and high Fe as resulting from partial melting at temperature conditions near the onset of biotite dehydration melting (e.g., Ward et al. 2008) and from peritectic Grt–Crd equilibrium. This is consistent with the presence of pinitized cordierite(?)–quartz intergrowths, which are texturally similar to the peritectic garnet–quartz intergrowths, also indicating its peritectic nature. Furthermore, even though Ca contents in garnet from S-type melts are typically low, peritectic garnets in high-pressure granulite-facies migmatites commonly display higher X_{Grs} with increasing pressure even in cases of partial melting of low Mg# metapelitic protoliths (e.g., Li et al. 2019). This further suggests partial melting at mid-crustal pressures.

The use of the Ti-in-quartz solubility model in estimating the pressures of quartz crystallization during early peritectic garnet crystallization yields widely varying pressures, from 8 to 10 kbar when considering high $aTiO_2$ (0.9, also used to calculate T_{Zirc}), to 6–7 kbar if lower $aTiO_2$ (0.5–0.4) are considered. The 8–10 kbar pressure range is significantly higher than that required for cordierite to be stable, and the pressure conditions of 6–7 kbar provide more reasonable estimates. This, however, implies variations in $aTiO_2$, which is common in evolving silicic melts (Teixeira et al. 2024). As such, considering varying $aTiO_2$ for quartz and zircon crystallization may provide a more realistic approach to the use of Ti-based geothermometers (Teixeira et al. 2024). Our quartz Ti contents are typically below 200, which suggest crystallization at $aTiO_2$ lower than 0.8 (Teixeira et al. 2024). The low Ti contents of the felsic volcanic rocks and our PAE modeling further suggests a low $aTiO_2$ for the melts, possibly due to efficient removal and/or lack of equilibrium of the melt and residual ilmenite, resulting in overall low $aTiO_2$ during the early partial melting reactions. After melt extraction from the source, however, cooling

and crystallization of other phases would likely result in increasing Ti contents of the melts (Teixeira et al. 2024).

The absence of additional $aTiO_2$ constraints, preserved minerals in equilibrium with garnet, the pervasive alteration and replacement of cordierite, and lack of whole-rock compositions that resemble the melt from which the phases crystallize hinders the use of garnet-based geothermometers or pseudosections to precisely constrain P–T conditions during partial melting. Nevertheless, the geothermobarometric constraints from zircon and quartz intergrown with garnet are consistent with peritectic garnet and cordierite crystallization during fluid-absent incongruent melting reactions involving biotite of a metasedimentary protolith in the middle crust (6–7 kbar), at temperature conditions near the onset of biotite incongruent melting reactions (*ca.* 820–870 ºC).

The major element zoning of the entrained peritectic garnets mimics common growth zonation of peritectic garnets generated during high-temperature incongruent partial melting reactions (Cesare 2000; Groppo et al. 2012). Garnet zoning is mainly controlled by the diffusion rate during growth (Clarke 1981). At temperatures below 640 ± 50 ºC, major element diffusion is negligible (Yardley 1977), whereas at temperatures above 700 ºC, diffusion rates of Fe, Mn and other major elements exponentially increase. Our Ti-in-zircon (T_{Zirc}) thermometry results indicate magmatic zircon crystallization at high temperatures, between *ca.* 690–870 ºC, but the preservation of garnet growth zoning suggests a limited residence time at high-T conditions (> 700 °C), preventing chemical exchange and interaction with the host melt. This further implies relatively fast extraction rates from the partial melting region and migration through the crust, which is possibly the cause of the intense garnet fracturing. This, however, would likely promote reaction with the melt and replacement. Given the lack of cordierite and/or biotite-dominated replacements of garnet along the fractures, it is also possible that garnet fracturing was due to increasing pressure (above lithostatic pressure) conditions, during magma recharge and eruption.

Additionally, the reduced estimated fO_2 magmatic conditions and the aluminous peritectic assemblages further indicate that the melt and peritectic phases were generated through the partial melting of reduced aluminous metasedimentary protoliths. Although melting of metagraywackes can produce garnet and cordierite as peritectic phases, in the range of the previously discussed P–T estimates (< 870 ºC and 6–7 kbar) orthopyroxene typically dominates peritectic assemblages (Vielzeuf and Montel 1994), indicating partial melting of a reduced aluminous pelitic source in the middle crust.

Such high-temperature melting processes in the middle crust indicates high geothermal gradients (above 40 ºC/km), a scenario previously suggested for the Paleozoic Iberian Pyrite Belt, a significantly base metal-endowed mining district (Tornos 2006). Such high geothermal gradients are likely induced by the mid to lower crustal emplacement of hot mantle-derived melts (Mitjavilla et al. 1997), providing the required heat to melt the crust, while deformation associated with the transtensional opening of the IPB basins may have further enhanced melt extraction and upper-crustal emplacement (Brown 2013; Clemens and Stevens 2016; Clemens et al. 2020; Johnson et al. 2021).

Preserved suprasolidus prograde monazite

Monazite in felsic magmatic rocks commonly grows during magma cooling and crystallization, after melt extraction from the source (Spear and Pyle 2010; Yakymchuk 2017). Suprasolidus prograde monazite has, nonetheless, been documented in migmatites (*e.g.,* Johnson et al. 2015; Blereau et al. 2016; Rocha et al. 2017).

The higher partitioning of Th into monazite in equilibrium with a melt (Xing et al. 2013) indicates that the high-Th monazite inclusions in the peritectic garnets and pinitized cordierite crystallized from a melt. Although the lack of monazite HREE data from the analyzed monazite grains hinders a complete assessment of the monazite-garnet equilibrium, the Y-rich composition of these inclusions further indicates monazite crystallization prior to peritectic garnet, as Y is highly compatible in garnet (*e.g.,* Pyle and Spear 2003). The Th–Y-rich monazite inclusions in peritectic garnets are thus interpreted as preserved prograde suprasolidus monazite, crystallized during earlier stages of partial melting. As temperature and melt connectivity increases in the partial melting area, prograde monazite is often subsequently dissolved into the melt (Yakymchuk 2017). However, the preservation potential of monazite can increase if included into co- or subsequently precipitated peritectic minerals, such as garnet. This is the mechanism most likely for the preservation of the suite of monazite grains included in garnet and pinitized cordierite. Therefore, the U–Pb monazite age of 356.8 ± 2.4 Ma is interpreted as representing the timing of peritectic garnet growth during partial melting reactions and overlaps within uncertainty with the with the *ca.* 360 Ma zircon population in the LA-ICP-MS dataset (Fig. 11), which we interpret as the timing of garnet growth. Although increasing evidence shows that the duration of partial melting and felsic melt extraction and emplacement processes are typically fast (< 1 Myr; Coulson et al. 2002; Devoir et al. 2021; Jung et al. 2022), felsic melts may also have long residence times in the lower to upper crust, prior to eruption (e.g., Cesare et al. 2003, 2009) as discussed below.

Eruption and preservation of peritectic phases

Our results clearly show that the erupted melts carried a significant amount of previously crystallized crystal cargo from older melt batches, which also fed voluminous eruptions. This attests to the presence of an upper-crustal reservoir that stored crystallized melts from previous voluminous crustal melt generation, storage and eruption episodes. Their preservation and eruption, however, requires that these phases survive subsequent melt recharge and extrusion, at *ca.* 345 Ma, after ca 15 Ma of storage below the solidus.

The lack of geochemical data from the youngest zircon grains hinders a complete assessment of some critical intensive parameter of the erupted melts such as temperature. Nevertheless, their clear K-poor and silicic nature, combined with the lower zircon saturation temperatures of the most silicic whole-rock compositions (700–770 ºC) suggests these melts were generated at lower temperatures and possibly from a biotite-poor source in the middle crust. This points to fluid-absent muscovite breakdown of a lower-grade protolith, which also commonly results in the crystallization of peritectic/residual K-feldspar (e.g., Dyck et al. 2019). Regardless of the nature of the source, the lower temperatures of the erupted melt would likely inhibit significant crystal cargo dissolution, offering a plausible explanation for the preservation of the abundant xenocrysts of older peritectic phases. Such scenario closely resembles the El Hoyazo dacites (Acosta-Vigil et al. 2010), which extruded at ca. 6 Ma a suite of remelted older (9 Ma) granulite-facies middle to lower crust glass-rich xenoliths, with abundant peritectic phases such as garnet and cordierite. As discussed in Acosta-Vigil et al (2010), the upper-crustal emplacement of felsic melts and entrained peritectic phases would largely induced melt crystallization, whereby subsequent water exsolution would remove most H_2O from the melt. As such, during subsequent voluminous magma recharge and consequent eruption of lower-temperature felsic magma, at *ca.* 345 Ma, melting, dissolution and replacement of the stored crystallized melts and peritectic phases would be inhibited, further promoting the preservation of the abundant xenoliths up to eruption.

Conclusions

In this study, we integrate geological, petrological, major and trace element whole-rock geochemical data of garnet-bearing rhyolites with major and trace element composition of garnet, Ti-in-quartz intergrown with garnet, trace element analysis and U–Pb isotopic dating of monazite and zircon to reach the following conclusions:

(1) Textural and chemical data from garnets-quartz intergrowths and smaller euhedral garnets clearly show that they represent entrained peritectic phases. These were generated during incongruent melting reactions involving biotite of a pelitic source in the middle crust, at temperatures up to 870 ºC.
(2) Garnet major element composition show homogenization by diffusion processes, but growth zoning is still preserved in large (up to 1 cm) garnet grains. The overall Fe-rich and Mg-poor composition of the peritectic garnets indicates compositional equilibrium with peritectic cordierite, which is also entrained and preserved as pinitized cordierite–quartz intergrowths.
(3) Despite the limited major element variation, garnets also exhibit prominent trace element oscillatory zoning and significant core-to-rim variations, recording the breakdown of biotite at high temperatures and also the dissolution of accessory phases during melting reactions.
(4) The preservation of the peritectic phases and lack of evidence for compositional modification via dissolution–reprecipitation processes suggests rapid melt extraction from the source, but also no significant compositional re-equilibration with the melt during extraction up to extrusion.
(5) The Th- and Y-rich monazite inclusions in peritectic garnet and cordierite are interpreted as preserved prograde suprasolidus monazite and place the timing of partial melting at 356.8 ± 2.4 Ma. This age overlaps with the 360 ± 1 Ma younger zircon population and represents one of the older major volcanic episodes in the region.
(6) Our data shows that the extruded silicic melts also carried a significant amount of pre-eruption zircon cargo, containing not only source-inherited zircon crystals, but also zircon that crystallized from previous moderate to high-temperature reduced felsic melts, possibly stored in an episodically and incrementally grown pluton, since *ca.* 390 Ma.
(7) The whole-rock geochemical data of the garnet-bearing volcanic rocks mainly reflects the entrainment of peritectic phases such as garnet, cordierite and K-feldspar, and our results thus show that a significant amount of xenoliths of peritectic and accessory phases from previously crystallized felsic melts were extruded along with a lower-temperature silicic magma, at ca. 345 Ma.
(8) This work further supports the view of protracted and incremental growth processes of magmatic reservoirs by accretion of several melt batches in a subsolidus low-temperature reservoir, which may be partly remo-

bilized and extruded during subsequent melt recharge and extrusion episodes.

Supplementary Information The online version contains supplementary material available at https://doi.org/10.1007/s00410-024-02106-3.

Acknowledgements The authors would like to thank Berit Løken Berg and Siri Simonsen (University of Oslo) for their assistance with sample characterization and assistance during LA-ICP-MS U–Pb work in Oslo, and the technical and administrative staff at the GeoLab-IGc-USP for assistance during sample preparation and analytical work in São Paulo. We also want to thank the support from the LNEG CEGMA team during the sampling campaigns. E. Ferreira and I. Dias da Silva are also thanked for helping with zircon separation. I. Martins is thanked for helping with the FC modeling and J. Cravinho and S. Pereira for help with graphic illustrations. We also want to thank J. Mata and T. B. dos Santos for comments on early versions of the manuscript. We are thankful to the reviewers W.J. Collins, M.J. Dorais and the Editor Dante Canil, whose thoughtful comments, suggestions, and reviews greatly improved this work. David Chew acknowledges support from Science Foundation Ireland (SFI) under Grant Number 13/RC/2092_P2 (iCRAG, the SFI Research Centre in Applied Geosciences). Karel Breiter acknowledges the support by RVO 67985831 at the Institute of Geology of the Czech Academy of Sciences. We are indebted to J-L. Paquette who sadly passed away during the preparation of this manuscript.

Funding Open access funding provided by FCT|FCCN (b-on). This work was funded by a research scholarship from SOMINCOR-Lunding Mining and two McKinstry Fund Society of Economic Geologists (SEG) Student Research Grants (SRG). This work was also supported by the Portuguese Fundação para a Ciência e a Tecnologia (FCT) I.P./MCTES through national funds (PIDDAC)–UIDB/50019/2020 (https://doi.org/https://doi.org/10.54499/UIDB/50019/2020), UIDP/50019/2020 (https://doi.org/https://doi.org/10.54499/UIDP/50019/2020) and LA/P/0068/2020 (https://doi.org/https://doi.org/10.54499/LA/P/0068/2020). A. Cravinho was financially supported by an IDL doctoral program FCT scholarship (PD/BD/142784/2018 and COVID/BD/152667/2022).

Data availability The data of this study are availabe in the Electronic Supplementatry Materials.

Declarations

Conflict of interest The authors declare that they have no conflicts of interest.

References

Abad I, Mata MP, Nieto F, Velilla N (2001) The phyllosilicates in diagenetic-metamorphic rocks of the South Portuguese Zone, southwestern Portugal. Can Mineral 39:1571–1589. https://doi.org/10.2113/gscanmin.39.6.1571

Acosta-Vigil A, Buick I, Hermann J et al (2010) Mechanisms of crustal anatexis: A geochemical study of partially melted metapelitic enclaves and host dacite, SE Spain. J Petrol 51:785–821. https://doi.org/10.1093/petrology/egp095

Acosta-Vigil A, London D, Morgan GB et al (2017) Primary crustal melt compositions: Insights into the controls, mechanisms and timing of generation from kinetics experiments and melt inclusions. Lithos 286–287:454–479. https://doi.org/10.1016/j.lithos.2017.05.020

Albardeiro L, Morais I, Matos JX et al (2023) Time-space evolution of Iberian Pyrite Belt igneous activity: Volcanic and plutonic lineaments, geochronology, ore horizons and stratigraphic constraints. Gondwana Res 121:235–258. https://doi.org/10.1016/j.gr.2023.05.004

Angiboust S, Harlov D (2017) Ilmenite breakdown and rutile-titanite stability in metagranitoids: Natural observations and experimental results. Am Mineral 102:1696–1708. https://doi.org/10.2138/am-2017-6064

Bachmann O, Miller CF, de Silva SL (2007) The volcanic-plutonic connection as a stage for understanding crustal magmatism. J Volcanol Geotherm Res 167:1–23. https://doi.org/10.1016/j.jvolgeores.2007.08.002

Bailie R, Adriaans L, le Roux P (2020) Peritectic assemblage entrainment as the main compositional driver in the I-type Vredenburg Granite, north-western Pan-African Saldania Belt, South Africa: A whole-rock chemical perspective. Lithos. https://doi.org/10.1016/j.lithos.2020.105522

Barbee O, Chesner C, Deering C (2020) Quartz crystals in Toba rhyolites show textures symptomatic of rapid crystallization. Am Mineral 105:194–226. https://doi.org/10.2138/am-2020-6947

Barbey P (2007) Diffusion-controlled biotite breakdown reaction textures at the solid/ liquid transition in the continental crust. Contrib to Mineral Petrol 154:707–716. https://doi.org/10.1007/s00410-007-0220-x

Barbey P, Marignac C, Montel JM et al (1999) Cordierite growth textures and the conditions of genesis and emplacement of crustal granitic magmas: The Velay granite complex (Massif Central, France). J Petrol 40:1425–1441. https://doi.org/10.1093/petroj/40.9.1425

Barrie TC, Amelin Y, Pascual E (2002) U-Pb geochronology of VMS mineralization in the Iberian Pyrite belt. Miner Depos 37:684–703. https://doi.org/10.1007/s00126-002-0302-7

Bell EA, Kirkpatrick HM (2021) Effects of crustal assimilation and magma mixing on zircon trace element relationships across the Peninsular Ranges Batholith. Chem Geol. https://doi.org/10.1016/j.chemgeo.2021.120616

Bell EA, Boehnke P, Barboni M, Harrison TM (2019) Tracking chemical alteration in magmatic zircon using rare earth element abundances. Chem Geol 510:56–71. https://doi.org/10.1016/j.chemgeo.2019.02.027

Black LP, Kamo SL, Allen CM et al (2004) Improved 206Pb/238U microprobe geochronology by the monitoring of a trace-element-related matrix effect; SHRIMP, ID–TIMS, ELA–ICP–MS and oxygen isotope documentation for a series of zircon standards. Chem Geol 205:115–140. https://doi.org/10.1016/j.chemgeo.2004.01.003

Blereau E, Clark C, Taylor RJM et al (2016) Constraints on the timing and conditions of high-grade metamorphism, charnockite formation and fluid-rock interaction in the Trivandrum Block,

southern India. J Metamorph Geol 34:527–549. https://doi.org/10.1111/jmg.12192
Blereau E, Johnson TE, Clark C et al (2017) Reappraising the P-T evolution of the Rogaland-Vest Agder Sector, southwestern Norway. Geosci Front 8:1–14. https://doi.org/10.1016/j.gsf.2016.07.003
Boehnke P, Watson EB, Trail D et al (2013) Zircon saturation re-revisited. Chem Geol 351:324–334. https://doi.org/10.1016/j.chemgeo.2013.05.028
Braid JA, Murphy JB, Quesada C, Mortensen J (2011) Tectonic escape of a crustal fragment during the closure of the Rheic Ocean: U-Pb detrital zircon data from the Late Palaeozoic Pulo do Lobo and South Portuguese zones, southern Iberia. J Geol Soc London 168:383–392. https://doi.org/10.1144/0016-76492010-104
Braid JA, Murphy JB, Quesada C et al (2012) Probing the composition of unexposed basement, South Portuguese Zone, southern Iberia: Implications for the connections between the Appalachian and Variscan orogens. Can J Earth Sci 49:591–613. https://doi.org/10.1139/E11-071
Breiter K, Novák M, Koller F, Cempírek J (2005) Phosphorus - An omnipresent minor element in garnet of diverse textural types from leucocratic granitic rocks. Mineral Petrol 85:205–221. https://doi.org/10.1007/s00710-005-0086-4
Brown M (2013) Granite: From genesis to emplacement. Bull Geol Soc Am 125:1079–1113. https://doi.org/10.1130/B30877.1
Bucholz CE, Stolper EM, Eiler JM, Breaks FW (2018) A Comparison of Oxygen Fugacities of Strongly Peraluminous Granites across the Archean-Proterozoic Boundary. J Petrol 59:2123–2156. https://doi.org/10.1093/petrology/egy091
Carvalho J, Inverno C, Matos JX et al (2017) Subsurface mapping in the Iberian Pyrite Belt using seismic reflection profiling and potential-field data. Int J Earth Sci 106:899–915. https://doi.org/10.1007/s00531-016-1340-1
Cesare B (2000) Incongruent melting of biotite to spinel in a quartz-free restite at El Joyazo (SE Spain): Textures and reaction characterization. Contrib to Mineral Petrol 139:273–284. https://doi.org/10.1007/s004100000137
Cesare B, Gómez-Pugnaire MT, Rubatto D (2003) Residence time of S-type anatectic magmas beneath the Neogene Volcanic Province of SE Spain: A zircon and monazite SHRIMP study. Contrib to Mineral Petrol 146:28–43. https://doi.org/10.1007/s00410-003-0490-x
Cesare B, Rubatto D, Gómez-Pugnaire MT (2009) Do extrusion ages reflect magma generation processes at depth? An example from the Neogene Volcanic Province of SE Spain. Contrib to Mineral Petrol 157:267–279. https://doi.org/10.1007/s00410-008-0333-x
Cesare B, Parisatto M, Mancini L et al (2021) Mineral inclusions are not immutable: Evidence of post-entrapment thermally-induced shape change of quartz in garnet. Earth Planet Sci Lett. https://doi.org/10.1016/j.epsl.2020.116708
Champion DC, Bultitude RJ (2013) The geochemical and SrNd isotopic characteristics of Paleozoic fractionated S-types granites of north Queensland: Implications for S-type granite petrogenesis. Lithos 162–163:37–56. https://doi.org/10.1016/j.lithos.2012.11.022
Chappell BW, White AJR (1992) I- and S-type granites in the Lachlan Fold Belt. Earth Environ Sci Trans R Soc Edinburgh 83:1–26. https://doi.org/10.1017/S0263593300007720
Charette B, Godet A, Guilmette C et al (2021) Long-lived anatexis in the exhumed middle crust of the Torngat Orogen: Constraints from phase equilibria modeling and garnet, zircon, and monazite geochronology. Lithos. https://doi.org/10.1016/j.lithos.2021.106022
Clarke DB (1981) The Mineralogy of Peraluminous Granites: A Review. Can Mineral 19:3–17
Clarke DB (1995) Cordierite in felsic igneous rocks: a synthesis. Mineral Mag 59:311–325. https://doi.org/10.1180/minmag.1995.059.395.15
Clarke DB (2007) Assimilation of xenocrysts in granitic magmas: principles, processes, proxies, and problems. Can Mineral 45:5–30. https://doi.org/10.2113/gscanmin.45.1.5
Clemens JD, Stevens G (2012) What controls chemical variation in granitic magmas? Lithos 134–135:317–329. https://doi.org/10.1016/j.lithos.2012.01.001
Clemens JD, Stevens G (2016) Melt segregation and magma interactions during crustal melting: Breaking out of the matrix. Earth-Science Rev 160:333–349. https://doi.org/10.1016/j.earscirev.2016.07.012
Clemens JD, Petford N, Mawer CK (1997) Ascent mechanisms of granitic magmas: causes and consequences. In: Holness MB (ed) Deformation-enhanced Fluid Transport in the Earth's Crust and Mantle. Chapman & Hall, London, pp 145–172
Clemens JD, Birch WD, Dudley RA (2011) S-type ignimbrites with polybaric crystallisation histories: The Tolmie Igneous Complex, Central Victoria, Australia. Contrib to Mineral Petrol 162:1315–1337. https://doi.org/10.1007/s00410-011-0652-1
Clemens JD, Buick IS, Kisters AFM, Frei D (2017a) Petrogenesis of the granitic Donkerhuk batholith in the Damara Belt of Namibia: protracted, syntectonic, short-range, crustal magma transfer. Contrib to Mineral Petrol 172:1–23. https://doi.org/10.1007/s00410-017-1370-0
Clemens JD, Stevens G, Frei D, Joseph CSA (2017b) Origins of cryptic variation in the Ediacaran-Fortunian rhyolitic ignimbrites of the Saldanha Bay Volcanic Complex, Western Cape, South Africa. Contrib to Mineral Petrol 172:1–23. https://doi.org/10.1007/s00410-017-1419-0
Clemens JD, Stevens G, Bryan SE (2020) Conditions during the formation of granitic magmas by crustal melting – Hot or cold; drenched, damp or dry? Earth-Science Rev. https://doi.org/10.1016/j.earscirev.2019.102982
Clemens JD, Bryan SE, Mayne MJ et al (2022) How are silicic volcanic and plutonic systems related? Part 1: A review of geological and geophysical observations, and insights from igneous rock chemistry. Earth-Science Rev. https://doi.org/10.1016/j.earscirev.2022.104249
Clemens JD, Stevens G, Coetzer LM (2023) Zircon inheritance, sources of Devonian granitic magmas and crustal structure in central Victoria. Aust J Earth Sci 70:227–259. https://doi.org/10.1080/08120099.2023.2139757
Codeço MS, Mateus A, Figueiras J et al (2018) Development of the Ervidel-Roxo and Figueirinha-Albernoa volcanic sequences in the Iberian pyrite Belt, Portugal: Metallogenic and geodynamic implications. Ore Geol Rev 98:80–108. https://doi.org/10.1016/j.oregeorev.2018.05.009
Corfu F, Hanchar JM, Hoskin PWO, Kinny P (2003) Atlas of Zircon Textures. Rev Mineral Geochemistry 53:469–500. https://doi.org/10.2113/0530469
Coulson IM, Villeneuve ME, Dipple GM et al (2002) Time-scales of assembly and thermal history of a composite felsic pluton: constraints from the Emerald Lake area, northern Canadian Cordillera, Yukon. J Volcanol Geotherm Res 114:331–356. https://doi.org/10.1016/S0377-0273(01)00294-3
Dahlquist JA, Galindo C, Pankhurst RJ et al (2007) Magmatic evolution of the Peñón Rosado granite: Petrogenesis of garnet-bearing granitoids. Lithos 95:177–207. https://doi.org/10.1016/j.lithos.2006.07.010
de Mello CR, Tornos F, Conde C et al (2022) Geology, Geochemistry, and Geochronology of the Giant Rio Tinto VMS Deposit, Iberian Pyrite Belt, Spain. Econ Geol 117:1149–1177. https://doi.org/10.5382/econgeo.4907

Devoir A, Bloch E, Müntener O (2021) Residence time of igneous garnet in Si-rich magmatic systems: Insights from diffusion modeling of major and trace elements. Earth Planet Sci Lett. https://doi.org/10.1016/j.epsl.2021.116771

Donaire T, Pascual E, Sáez R et al (2020a) Geochemical and Nd isotopic signature of felsic volcanic rocks as a proxy of volcanic-hosted massive sulphide deposits in the Iberian Pyrite Belt (SW, Spain): The Paymogo Volcano-Sedimentary Alignment. Ore Geol Rev. https://doi.org/10.1016/j.oregeorev.2020.103408

Donaire T, Pascual E, Sáez R, Toscano M (2020b) Facies architecture and palaeoenvironmental constraints of subaqueous felsic volcanism in the Iberian Pyrite Belt: The Paymogo Volcano-Sedimentary Alignment. J Volcanol Geotherm Res. https://doi.org/10.1016/j.jvolgeores.2020.107045

Dorais MJ, Campbell S (2022) Peritectic and phenocrystic garnet accumulation and the origin of strongly peraluminous granitic rocks: The Flagstaff Lake Igneous Complex. Maine Lithos. https://doi.org/10.1016/j.lithos.2022.106680

Dorais MJ, Campbell S (2023) An oxygen isotopic study of garnet and zircon of the Flagstaff Lake Igneous Complex: Identification of peritectic and phenocrystic garnet with implications for the petrogenesis of strongly peraluminous granites. Lithos. https://doi.org/10.1016/j.lithos.2023.107042

Dorais MJ, Spencer CJ (2014) Revisiting the importance of residual source material (restite) in granite petrogenesis: The Cardigan Pluton, New Hampshire. Lithos 202–203:237–249. https://doi.org/10.1016/j.lithos.2014.05.007

Dorais MJ, Tubrett M (2012) Detecting peritectic garnet in the peraluminous Cardigan pluton, New Hampshire. J Petrol 53:299–324. https://doi.org/10.1093/petrology/egr063

Dyck B, Waters DJ, St-Onge MR, Searle MP (2019) Muscovite dehydration melting; reaction mechanisms, microstructures, and implications for anatexis. J Metamorph Geol. https://doi.org/10.1111/jmg.12511

Erdmann S, Jamieson RA, MacDonald MA (2009) Evaluating the origin of garnet, cordierite, and biotite in granitic rocks: A case study from the South Mountain Batholith, Nova Scotia. J Petrol 50:1477–1503. https://doi.org/10.1093/petrology/egp038

Farina F, Stevens G, Dini A, Rocchi S (2012) Peritectic phase entrainment and magma mixing in the late Miocene Elba Island laccolith-pluton-dyke complex (Italy). Lithos 153:243–260. https://doi.org/10.1016/j.lithos.2012.05.011

Ferreira JA, Bento dos Santos T, Pereira I, Mata J (2019) Tectonically assisted exhumation and cooling of Variscan granites in an anatectic complex of the Central Iberian Zone, Portugal: constraints from LA-ICP-MS zircon and apatite U-Pb ages. Int J Earth Sci 108:2153–2175. https://doi.org/10.1007/s00531-019-01755-1

Ferrero S, Bartoli O, Cesare B et al (2012) Microstructures of melt inclusions in anatectic metasedimentary rocks. J Metamorph Geol 30:303–322. https://doi.org/10.1111/j.1525-1314.2011.00968.x

Ferry JM, Watson EB (2007) New thermodynamic models and revised calibrations for the Ti-in-zircon and Zr-in-rutile thermometers. Contrib to Mineral Petrol 154:429–437. https://doi.org/10.1007/s00410-007-0201-0

Fiannacca P, Williams IS, Cirrincione R (2017) Timescales and mechanisms of batholith construction: Constraints from zircon oxygen isotopes and geochronology of the late Variscan Serre Batholith (Calabria, southern Italy). Lithos 277:302–314. https://doi.org/10.1016/j.lithos.2016.06.011

Garcia-Arias M, Stevens G (2017) Phase equilibrium modelling of granite magma petrogenesis: B. An evaluation of the magma compositions that result from fractional crystallization. Lithos 277:109–130. https://doi.org/10.1016/j.lithos.2016.09.027

Gasquet D, Bertrand J-M, Paquette J-L et al (2010) Miocene to Messinian deformation and hydrothermal activity in a pre-Alpine basement massif of the French western Alps: new U-Th-Pb and argon ages from the Lauzière massif. Bull La Société Géologique Fr 181:227–241. https://doi.org/10.2113/gssgfbull.181.3.227

Gonçalves GO, Lana C, Scholz R et al (2016) An assessment of monazite from the Itambé pegmatite district for use as U-Pb isotope reference material for microanalysis and implications for the origin of the "Moacyr" monazite. Chem Geol 424:30–50. https://doi.org/10.1016/j.chemgeo.2015.12.019

Goncalves P, Raimondo T, Paquette J, de Souza S, de Oliveira J (2021) Garnet as a monitor for melt–rock interaction: Textural, mineralogical, and compositional evidence of partial melting and melt-driven metasomatism. J Metamorph Geol 39:617–648. https://doi.org/10.1111/jmg.12592

Green TH (1977) Mineralogy and Petrology Garnet in Silicic Liquids and Its Possible Use as a P - T. Mineral Petrol 67:59–67

Groppo C, Rolfo F, Indares A (2012) Partial melting in the higher Himalayan crystallines of Eastern Nepal: The effect of decompression and implications for the "channel flow" model. J Petrol 53:1057–1088. https://doi.org/10.1093/petrology/egs009

Groppo C, Rolfo F, Mosca P (2013) The cordierite-bearing anatectic rocks of the higher Himalayan crystallines (eastern Nepal): Low-pressure anatexis, melt productivity, melt loss and the preservation of cordierite. J Metamorph Geol 31:187–204. https://doi.org/10.1111/jmg.12014

Harangi S, Downes H, Kósa L et al (2002) Almandine Garnet in Calc-alkaline Volcanic Rocks of the Northern Pannonian Basin (Eastern–Central Europe): Geochemistry, Petrogenesis and Geodynamic Implications. J Petrol 42:1813–1843. https://doi.org/10.1093/petrology/42.10.1813

Hensen BJ, Green DH (1972) Experimental study of the stability of cordierite and garnet in pelitic compositions at high pressures and temperatures - II. Compositions without excess alumino-silicate. Contrib to Mineral Petrol 35:331–354. https://doi.org/10.1007/BF00371314

Holdaway MJ, Lee SM (1977) Fe-Mg cordierite stability in high-grade pelitic rocks based on experimental, theoretical, and natural observations. Contrib to Mineral Petrol 63:175–198. https://doi.org/10.1007/BF00398778

Holder RM, Yakymchuk C, Viete DR (2020) Accessory Mineral Eu Anomalies in Suprasolidus Rocks: Beyond Feldspar. Geochemistry, Geophys Geosystems 21:1–16. https://doi.org/10.1029/2020GC009052

Huang X-D, Huang D, Lu J-J et al (2023) Neoproterozoic tungsten mineralization: Geology, chronology, and genesis of the Huashandong W deposit in northwestern Jiangxi, South China. Miner Depos 58:771–796. https://doi.org/10.1007/s00126-022-01157-5

Jochum KP, Weis U, Stoll B et al (2011) Determination of Reference Values for NIST SRM 610–617 Glasses Following ISO Guidelines. Geostand Geoanalytical Res 35:397–429. https://doi.org/10.1111/j.1751-908X.2011.00120.x

Johnson TE, Clark C, Taylor RJM et al (2015) Prograde and retrograde growth of monazite in migmatites: An example from the Nagercoil Block, southern India. Geosci Front 6:373–387. https://doi.org/10.1016/j.gsf.2014.12.003

Johnson T, Yakymchuk C, Brown M (2021) Crustal melting and suprasolidus phase equilibria: From first principles to the state-of-the-art. Earth-Science Rev. https://doi.org/10.1016/j.earscirev.2021.103778

Jung S, Pfänder JA, Mezger K et al (2022) Polyphase growth history of peritectic garnet from a granite: Trace-element zonation. Lithos, Lu-Hf ages and their significance for the duration of granite-forming processes. https://doi.org/10.1016/j.lithos.2022.106675

Konrad-Schmolke M, Halama R, Chew D et al (2022) Discrimination of thermodynamic and kinetic contributions to the heavy rare earth element patterns in metamorphic garnet. J Metamorph Geol. https://doi.org/10.1111/jmg.12703

Lains Amaral J, Rita Solá A, Bento dos Santos TM et al (2021) U-Pb zircon SHRIMP dating of a protracted magmatic setting and its volcanic emplacement: insights from the felsic volcanic rocks hosting the sulphide ore of the giant Aljustrel Deposit. Ore Geol Rev, Iberian Pyrite Belt. https://doi.org/10.1016/j.oregeorev.2021.104147

Large SJE, Wotzlaw J-F, Guillong M et al (2020) Resolving the timescales of magmatic and hydrothermal processes associated with porphyry deposit formation using zircon U-Pb petrochronology. Geochronology 2:209–230. https://doi.org/10.5194/gchron-2-209-2020

Lavaure S, Sawyer EW (2011) Source of biotite in the Wuluma Pluton: Replacement of ferromagnesian phases and disaggregation of enclaves and schlieren. Lithos 125:757–780. https://doi.org/10.1016/j.lithos.2011.04.005

Li X, White RW, Wei C (2019) Can we extract ultrahigh-temperature conditions from Fe-rich metapelites? An example from the Khondalite Belt, North China Craton. Lithos 328–329:228–243. https://doi.org/10.1016/j.lithos.2019.01.032

Li X-Y, Lu J-J, Zhang R-Q et al (2021) Magma evolution leading to veinlet-disseminated tungsten mineralization at the Muguayuan deposit: In-situ analysis of igneous minerals. Ore Geol Rev. https://doi.org/10.1016/j.oregeorev.2021.104406

Locock AJ (2008) An Excel spreadsheet to recast analyses of garnet into end-member components, and a synopsis of the crystal chemistry of natural silicate garnets. Comput Geosci 34:1769–1780. https://doi.org/10.1016/j.cageo.2007.12.013

Loucks RR, Fiorentini ML, Henríquez GJ (2020) New Magmatic Oxybarometer Using Trace Elements in Zircon. J Petrol. https://doi.org/10.1093/petrology/egaa034

Lucci F, Rossetti F, Becchio R et al (2018) Magmatic Mn-rich garnets in volcanic settings: Age and longevity of the magmatic plumbing system of the Miocene Ramadas volcanism (NW Argentina). Lithos 322:238–249. https://doi.org/10.1016/j.lithos.2018.10.016

Ludwig KR (2003) A Geochronological Toolkit for Microsoft Excel. Berkeley Geochronol Center, Spec Publ 4:71

Ludwig KR (2009) SQUID 2: A User's Manual. Berkeley Geochronology Center Special Publication

Luvizotto GL, Zack T, Triebold S, Von Eynatten H (2009) Rutile occurrence and trace element behavior in medium-grade metasedimentary rocks: Example from the Erzgebirge, Germany. Mineral Petrol 97:233–249. https://doi.org/10.1007/s00710-009-0092-z

Luz F, Mateus A, Ferreira E et al (2021) Pb-Nd-Sr Isotope Geochemistry of Metapelites from the Iberian Pyrite Belt and Its Relevance to Provenance Analysis and Mineral Exploration Surveys. Econ Geol. https://doi.org/10.5382/econgeo.4869

Maner JL, London D, Icenhower JP (2019) Enrichment of manganese to spessartine saturation in granite-pegmatite systems. Am Mineral 104:1625–1637. https://doi.org/10.2138/am-2019-6938

Manor MJ, Piercey SJ, Wall CJ (2023) Zircon and the role of magmatic petrogenesis in the formation of felsic-hosted volcanogenic massive sulfide (VMS) deposits: a case study from the mid-Paleozoic Yukon-Tanana terrane, northern Canadian Cordillera. Miner Depos. https://doi.org/10.1007/s00126-023-01213-8

McDonough WF, Sun S (1995) The composition of the Earth. Chem Geol 120:223–253. https://doi.org/10.1016/0009-2541(94)00140-4

McPhie J, Doyle MG, Allen RL (1993) Volcanic Textures: A guide to the interpretation of textures in volcanic rocks. University of Tasmania, Hobart, Centre for Ore Deposit and Exploration Studies

Mendes M, Pereira Z, Matos JX et al (2020) New insights on the middle Givetian/middle Frasnian palynofloras from the Phyllite-Quartzite Formation in the Neves-Corvo mine region (Iberian Pyrite Belt, Portugal). Rev Micropaleontol. https://doi.org/10.1016/j.revmic.2020.100447

Mitjavila J, Martí J, Soriano G (1997) Magmatic evolution and tectonic setting of the Iberian Pyrite Belt volcanism. J Petrol 38:727–755. https://doi.org/10.1093/petroj/38.6.727

Munhá J (1990) Metamorphic Evolution of the South Portuguese/Pulo Do Lobo Zone. In: Dallmeyer RD, Garcia EM (eds) Pre-Mesozoic Geology of Iberia. Springer, Berlin Heidelberg, Berlin, Heidelberg, pp 363–368

Murphy JB, Hamilton MA (2000) Orogenesis and Basin Development: U-Pb Detrital Zircon Age Constraints on Evolution of the Late Paleozoic St. Marys Basin. Central Mainland Nova Scotia J Geol 108:53–71. https://doi.org/10.1086/314384

Nance RD, Gutiérrez-Alonso G, Keppie JD et al (2012) A brief history of the Rheic Ocean. Geosci Front 3:125–135. https://doi.org/10.1016/j.gsf.2011.11.008

Narduzzi F, Farina F, Stevens G et al (2017) Magmatic garnet in the Cordilleran-type Galiléia granitoids of the Araçuaí belt (Brazil): Evidence for crystallization in the lower crust. Lithos 282–283:82–97. https://doi.org/10.1016/j.lithos.2017.02.017

Nasdala L, Corfu F, Schoene B et al (2018) GZ7 and GZ8 - Two Zircon Reference Materials for SIMS U-Pb Geochronology. Geostand Geoanalytical Res 42:431–457. https://doi.org/10.1111/ggr.12239

Nazari-Dehkordi T, Robb L (2022) Zircon mineral chemistry and implications for magmatic-hydrothermal evolution of the granite-hosted Zaaiplaats Sn deposit, Bushveld Large Igneous Province. South Africa Lithos. https://doi.org/10.1016/j.lithos.2022.106672

Oliveira JT, Pereira Z, Carvalho P et al (2004) Stratigraphy of the tectonically imbricated lithological succession of the Neves Corvo mine area, Iberian Pyrite Belt, Portugal. Miner Depos 39:422–436. https://doi.org/10.1007/s00126-004-0415-2

Oliveira JT, Rosa CJP, Pereira Z et al (2013) Geology of the Rosário-Neves Corvo antiform, Iberian Pyrite Belt, Portugal: New insights from physical volcanology, palynostratigraphy and isotope geochronology studies. Miner Depos 48:749–766. https://doi.org/10.1007/s00126-012-0453-0

Oliveira JT, Quesada C, Pereira Z, et al (2019) South Portuguese Terrane: A Continental Affinity Exotic Unit. In: Quesada C, Oliveira JT (eds) The Geology of Iberia: A Geodynamic Approach. Springer Nature, pp 173–206

Oliveira JT (1990) South Portuguese Zone: introduction. Stratigraphy and synsedimentary tectonism. In: Dallmeyer RD, Martinez GE (eds) PreMesozoic Geology of Iberia. Springer-Verlag, pp 333–347

Osborne ZR, Thomas JB, Nachlas WO et al (2022) TitaniQ revisited: expanded and improved Ti-in-quartz solubility model for thermobarometry. Contrib Mineral Petrol. https://doi.org/10.1007/s00410-022-01896-8

Palme H, O'Neill HSC (2014) 3.1: Cosmochemical Estimates of Mantle Composition. In: Holland HD, Turekian KKBT-T on G (Second E (eds). Elsevier, Oxford, pp 1–39

Paquette J-L, Piro J-L, Devidal J-L, et al (2014) Sensitivity Enhancement in LA-ICP-MS by N2 Addition to Carrier Gas: Application to Radiometric Dating of U-Th-Bearing Minerals. Agil ICP-MS J 4–5

Pastor-Galán D, Gutiérrez-Alonso G, Weil AB (2020) The enigmatic curvature of Central Iberia and its puzzling kinematics. Solid Earth 11:1247–1273. https://doi.org/10.5194/se-11-1247-2020

Paton C, Hellstrom J, Paul B et al (2011) Iolite: Freeware for the visualisation and processing of mass spectrometric data. J Anal at Spectrom 26:2508. https://doi.org/10.1039/c1ja10172b

Pereira Z, Matos JX, Fernandes P, Oliveira JT (2007) Devonian and Carboniferous palynostratigraphy of the South Portuguese Zone, Portugal - An overview. Comun Geol 94:53–79

Pereira Z, Matos JX, Solá AR, et al (2021) Geology of the recently discovered massive and stockwork sulphide mineralization at Semblana, Rosa Magra and Monte Branco, Neves-Corvo mine region, Iberian Pyrite Belt, Portugal. Geol Mag https://doi.org/10.1017/S0016756820001284

Pichavant M, Kontak DJ, Briqueu L et al (1988) The Miocene-Pliocene Macusani Volcanics, SE Peru - II. Geochemistry and origin of a felsic peraluminous magma. Contrib to Mineral Petrol 100:325–338. https://doi.org/10.1007/BF00379742

Pichavant M, Erdmann S, Kontak DJ et al (2024) Trace element partitioning in strongly peraluminous rare-metal silicic magmas – Implications for fractionation processes and for the origin of the Macusani Volcanics (SE Peru). Geochim Cosmochim Acta 365:229–252. https://doi.org/10.1016/j.gca.2023.11.021

Pineda C, Schmitt AK, Morata D (2022) Monazite as a control on Th/U in magmatic zircon. Chem Geol. https://doi.org/10.1016/j.chemgeo.2022.120911

Plümper O, Putnis A (2009) The complex hydrothermal history of granitic rocks: Multiple feldspar replacement reactions under subsolidus conditions. J Petrol 50:967–987. https://doi.org/10.1093/petrology/egp028

Pyle JM, Spear FS (2003) Yttrium zoning in garnet: Coupling of major and accessory phases during metamorphic reactions. Am Mineral 88:708

Quesada C (1991) Geological constraints on the Paleozoic tectonic evolution of tectonostratigraphic terranes in the Iberian Massif. Tectonophysics 185:225–245. https://doi.org/10.1016/0040-1951(91)90446-Y

Ribeiro A, Munhá J, Dias R et al (2007) Geodynamic evolution of the SW Europe Variscides. Tectonics 26:1–24. https://doi.org/10.1029/2006TC002058

Ribeiro A, Munhá J, Fonseca PE et al (2010) Variscan ophiolite belts in the Ossa-Morena Zone (Southwest Iberia): Geological characterization and geodynamic significance. Gondwana Res 17:408–421. https://doi.org/10.1016/j.gr.2009.09.005

Rocha BC, Moraes R, Möller A et al (2017) Timing of anatexis and melt crystallization in the Socorro-Guaxupé Nappe, SE Brazil: Insights from trace element composition of zircon, monazite and garnet coupled to U-Pb geochronology. Lithos 277:337–355. https://doi.org/10.1016/j.lithos.2016.05.020

Rong W, Zhang SB, Zheng YF (2017) Back-reaction of peritectic garnet as an explanation for the origin of mafic enclaves in S-type granite from the Jiuling batholith in South China. J Petrol 58:569–598. https://doi.org/10.1093/petrology/egx029

Rosa CJP, McPhie J, Relvas JMRS et al (2008) Facies analyses and volcanic setting of the giant Neves Corvo massive sulfide deposit, Iberian Pyrite Belt, Portugal. Miner Depos 43:449–466. https://doi.org/10.1007/s00126-008-0176-4

Rosa DRN, Finch AA, Andersen T, Inverno CMC (2009) U-Pb geochronology and Hf isotope ratios of magmatic zircons from the Iberian Pyrite Belt. Mineral Petrol 95:47–69. https://doi.org/10.1007/s00710-008-0022-5

Rubatto D, Burger M, Lanari P et al (2020) Identification of growth mechanisms in metamorphic garnet by high-resolution trace element mapping with LA-ICP-TOFMS. Contrib to Mineral Petrol 175:1–19. https://doi.org/10.1007/s00410-020-01700-5

Samadi R, Miller NR, Mirnejad H et al (2014) Origin of garnet in aplite and pegmatite from Khajeh Morad in northeastern Iran: A major, trace element, and oxygen isotope approach. Lithos 208:378–392. https://doi.org/10.1016/j.lithos.2014.08.023

Sambridge MS, Compston W (1994) Mixture modeling of multi-component data sets with application to ion-probe zircon ages. Earth Planet Sci Lett 128:373–390. https://doi.org/10.1016/0012-821X(94)90157-0

Sato K, Tassinari CCG, Basei MAS et al (2014) Sensitive High Resolution Ion Microprobe (SHRIMP IIe/MC) of the Institute of Geosciences of the University of São Paulo, Brazil: analytical method and first results. Geol USP Série Científica 14:3–18. https://doi.org/10.5327/Z1519-874X201400030001

Scallion KL, Jamieson RA, Barr SM et al (2011) Texture and composition of garnet as a guide to contamination of granitoid plutons: An example from the Governor Lake area, Meguma terrane, Nova Scotia. Can Mineral 49:441–458. https://doi.org/10.3749/canmin.49.2.441

Schiller D, Finger F (2019) Application of Ti-in-zircon thermometry to granite studies: problems and possible solutions. Contrib Mineral Petrol 174:1–16. https://doi.org/10.1007/s00410-019-1585-3

Schönig J, von Eynatten H, Tolosana-Delgado R, Meinhold G (2021) Garnet major-element composition as an indicator of host-rock type: a machine learning approach using the random forest classifier. Contrib Mineral Petrol 176:98. https://doi.org/10.1007/s00410-021-01854-w

Seydoux-Gillaume AM, Montel JM, Paquette JL, Marinho M (1999) Experimental study of the resetting of the U-Th-Pb geochronological system of monazite. EUG X Terra 1:800

Seydoux-Guillaume A-M, Paquette J-L, Wiedenbeck M et al (2002) Experimental resetting of the U-Th–Pb systems in monazite. Chem Geol 191:165–181. https://doi.org/10.1016/S0009-2541(02)00155-9

Shellnutt JG, Owen JV, Yeh MW et al (2019) Long-lived association between Avalonia and the Meguma terrane deduced from zircon geochronology of metasedimentary granulites. Sci Rep 9:1–11. https://doi.org/10.1038/s41598-019-40673-9

Sieck P, López-Doncel R, Dávila-Harris P et al (2019) Almandine garnet-bearing rhyolites associated to bimodal volcanism in the Mesa Central of Mexico: Geochemical, petrological and geochronological evolution. J South Am Earth Sci 92:310–328. https://doi.org/10.1016/j.jsames.2019.03.018

Spear FS, Pyle JM (2010) Theoretical modeling of monazite growth in a low-Ca metapelite. Chem Geol 273:111–119. https://doi.org/10.1016/j.chemgeo.2010.02.016

Spear FS, Kohn MJ, Cheney JT (1999) P: T paths from anatectic pelites. Contrib to Mineral Petrol 134:17–32. https://doi.org/10.1007/s004100050466

Stacey JS, Kramers JD (1975) Approximation of terrestrial lead isotope evolution by a two-stage model. Earth Planet Sci Lett 26:207–221. https://doi.org/10.1016/0012-821X(75)90088-6

Stepanov A, Mavrogenes JA, Meffre S, Davidson P (2014) The key role of mica during igneous concentration of tantalum. Contrib Mineral Petrol 167:1–8. https://doi.org/10.1007/s00410-014-1009-3

Stevens G, Villaros A, Moyen JF (2007) Selective peritectic garnet entertainment as the origin of geochemical diversity in S-type granites. Geology 35:9–12. https://doi.org/10.1130/G22959A.1

Sun K-K, Deng J, Wang Q-F et al (2023) Formation of Sn-rich granitic magma: a case study of the highly evolved Kafang granite in the Gejiu tin polymetallic ore district, South China. Miner Depos 58:359–378. https://doi.org/10.1007/s00126-022-01130-2

Taylor J, Stevens G (2010) Selective entrainment of peritectic garnet into S-type granitic magmas: Evidence from Archaean mid-crustal anatectites. Lithos 120:277–292. https://doi.org/10.1016/j.lithos.2010.08.015

Taylor J, Stevens G, Armstrong R, Kisters AFM (2010) Granulite facies anatexis in the Ancient Gneiss Complex, Swaziland, at 2.73 Ga: Mid-crustal metamorphic evidence for mantle heating of the Kaapvaal craton during Ventersdorp magmatism. Precambrian Res 177:88–102. https://doi.org/10.1016/j.precamres.2009.11.005

Taylor RJM, Harley SL, Hinton RW et al (2015) Experimental determination of REE partition coefficients between zircon, garnet and melt: a key to understanding high-T crustal processes. J Metamorph Geol 33:231–248. https://doi.org/10.1111/jmg.12118

Teixeira LMF, Troch J, Bachmann O (2024) The dynamic nature of a TiO2: Implications for Ti-based thermometers in magmatic systems. Geology 52:92–96. https://doi.org/10.1130/G51587.1

Tomascak PB, Krogstad EJ, Walker RJ (1996) U-Pb Monazite Geochronology of Granitic Rocks from Maine: Implications for Late Paleozoic Tectonics in the Northern Appalachians. J Geol 104:185–195. https://doi.org/10.1086/629813

Tornos F (2006) Environment of formation and styles of volcanogenic massive sulfides: The Iberian Pyrite Belt. Ore Geol Rev 28:259–307. https://doi.org/10.1016/j.oregeorev.2004.12.005

Tornos F, Casquet C, Relvas JMRS et al (2002) The relationship between ore deposits and oblique tectonics: the SW Iberian Variscan Belt. Geol Soc London, Spec Publ 204:179–198. https://doi.org/10.1144/GSL.SP.2002.204.01.11

Ubide T, McKenna CA, Chew DM, Kamber BS (2015) High-resolution LA-ICP-MS trace element mapping of igneous minerals: In search of magma histories. Chem Geol 409:157–168. https://doi.org/10.1016/j.chemgeo.2015.05.020

Valenzuela A, Donaire T, Pin C et al (2011) Geochemistry and U-Pb dating of felsic volcanic rocks in the Riotinto-Nerva unit, Iberian Pyrite Belt, Spain: crustal thinning, progressive crustal melting and massive sulphide genesis. J Geol Soc London 168:717–732. https://doi.org/10.1144/0016-76492010-081

Vielzeuf D, Montel JM (1994) Partial melting of metagreywackes. Part I. Fluid-absent experiments and phase relationships. Contrib to Mineral Petrol 117:375–393. https://doi.org/10.1007/BF00307272

Vielzeuf D, Schmidt MW (2001) Melting relations in hydrous systems revisited: Application to metapelites, metagreywackes and metabasalts. Contrib to Mineral Petrol 141:251–267. https://doi.org/10.1007/s004100100237

Villaros A, Stevens G, Buick IS (2009a) Tracking S-type granite from source to emplacement: Clues from garnet in the Cape Granite Suite. Lithos 112:217–235. https://doi.org/10.1016/j.lithos.2009.02.011

Villaros A, Stevens G, Moyen JF, Buick IS (2009b) The trace element compositions of S-type granites: Evidence for disequilibrium melting and accessory phase entrainment in the source. Contrib to Mineral Petrol 158:543–561. https://doi.org/10.1007/s00410-009-0396-3

Villaros A, Buick IS, Stevens G (2012) Isotopic variations in S-type granites: An inheritance from a heterogeneous source? Contrib to Mineral Petrol 163:243–257. https://doi.org/10.1007/s00410-011-0673-9

Vogt M, Schwarz WH, Schmitt AK et al (2023) Graphitic inclusions in zircon from early Phanerozoic S-type granite: Implications for the preservation of Hadean biosignatures. Geochim Cosmochim Acta 349:23–40. https://doi.org/10.1016/j.gca.2023.03.022

Waldron JWF, White CE, Barr SM et al (2009) Provenance of the Meguma terrane, Nova Scotia: rifted margin of early Paleozoic Gondwana. Can J Earth Sci 46:1–8. https://doi.org/10.1139/E09-004

Wallrich BM, Miller CF, Gualda GAR et al (2023) Volcano-pluton connection: Perspectives on material and process linkages, Searchlight pluton and Highland Range volcanic sequence, Nevada, USA. Earth-Science Rev. https://doi.org/10.1016/j.earscirev.2023.104361

Wark DA, Watson EB (2006) TitaniQ: A titanium-in-quartz geothermometer. Contrib to Mineral Petrol 152:743–754. https://doi.org/10.1007/s00410-006-0132-1

Waters DJ (2001) The significance of prograde and retrograde quartz-bearing intergrowth microstructures in partially melted granulite-facies rocks. Lithos 56:97–110. https://doi.org/10.1016/s0024-4937(00)00061-x

Watson EB, Harrison TM (1983) Zircon saturation revisited: temperature and composition effects in a variety of crustal magma types. Earth Planet Sci Lett 64:295–304. https://doi.org/10.1016/0012-821X(83)90211-X

White RW, Powell R (2002) Melt loss and the preservation of granulite facies mineral assemblages. J Metamorph Geol 20:621–632. https://doi.org/10.1046/j.1525-1314.2002.00206.x

White RW, Powell R, Halpin JA (2004) Spatially-focussed melt formation in aluminous metapelites from Broken Hill, Australia. J Metamorph Geol 22:825–845. https://doi.org/10.1111/j.1525-1314.2004.00553.x

White RW, Powell R, Holland TJB et al (2014a) New mineral activity–composition relations for thermodynamic calculations in metapelitic systems. J Metamorph Geol 32:261–286. https://doi.org/10.1111/jmg.12071

White RW, Powell R, Johnson TE (2014b) The effect of Mn on mineral stability in metapelites revisited: New a-x relations for manganese-bearing minerals. J Metamorph Geol 32:809–828. https://doi.org/10.1111/jmg.12095

Wiedenbeck M, Allé P, Corfu F et al (1995) Three Natural Zircon Standards for U-Th-Pb, Lu-Hf, trace element and REE analyses. Geostand Geoanalytical Res 19:1–23. https://doi.org/10.1111/j.1751-908X.1995.tb00147.x

Wiedenbeck M, Hanchar JM, Peck WH et al (2004) Further Characterisation of the 91500 Zircon Crystal. Geostand Geoanalytical Res 28:9–39. https://doi.org/10.1111/j.1751-908X.2004.tb01041.x

Williams IS (1997) U-Th-Pb Geochronology by Ion Microprobe. In: Applications of Microanalytical Techniques to Understanding Mineralizing Processes. Society of Economic Geologists, pp 1–35

Xing L, Trail D, Watson EB (2013) Th and U partitioning between monazite and felsic melt. Chem Geol 358:46–53. https://doi.org/10.1016/j.chemgeo.2013.07.009

Yakymchuk C (2017) Behaviour of apatite during partial melting of metapelites and consequences for prograde suprasolidus monazite growth. Lithos 274–275:412–426. https://doi.org/10.1016/j.lithos.2017.01.009

Yakymchuk C, Brown M, Clark C et al (2015) Decoding polyphase migmatites using geochronology and phase equilibria modelling. J Metamorph Geol 33:203–230. https://doi.org/10.1111/jmg.12117

Yang P, Rivers T (2000) Trace element partitioning between coexisting biotite and muscovite from metamorphic rocks, Western Labrador: structural, compositional and thermal controls. Geochim Cosmochim Acta 64:1451–1472. https://doi.org/10.1016/S0016-7037(99)00425-1

Yardley BWD (1977) An empirical study of diffusion in garnet. Am Mineral 62:793–800

Zhang C, Giere R, Stiinitz H et al (2001) Garnet–quartz intergrowths in granitic pegmatites from Bergell and Adamello, Italy. Schweizerisc Mineral Petrogr Mitteil 81:89–113

Zhu Y, Lai S, Qin J et al (2020) Petrogenesis and geochemical diversity of Late Mesoproterozoic S-type granites in the western Yangtze Block, South China: Co-entrainment of peritectic selective phases and accessory minerals. Lithos. https://doi.org/10.1016/j.lithos.2019.105326

Zhu Y, Cong LS, Feng QJ et al (2021) Peritectic assemblage entrainment (PAE) model for the petrogenesis of Neoproterozoic high-maficity I-type granitoids in the western Yangtze Block. Lithos, South China. https://doi.org/10.1016/j.lithos.2021.106247